Remote Sensing of Environment 273 (2022) 112986

Contents lists available at ScienceDirect

Remote Sensing of Environment

journal homepage: www.elsevier.com/locate/rse

Evaluation of SIF retrievals from narrow-band and sub-nanometer airborne hyperspectral imagers flown in tandem: Modelling and validation in the context of plant phenotyping

A. Belwalkar [a], T. Poblete [a], A. Longmire [b], A. Hornero [c,d], R. Hernandez-Clemente [d], P. J. Zarco-Tejada [a,b,c,*]

[a] *Department of Infrastructure Engineering, Faculty of Engineering and Information Technology (FEIT), University of Melbourne, Melbourne, Victoria, Australia*
[b] *School of Agriculture and Food, Faculty of Veterinary and Agricultural Sciences (FVAS), University of Melbourne, Melbourne, Victoria, Australia*
[c] *Instituto de Agricultura Sostenible (IAS), Consejo Superior de Investigaciones Científicas (CSIC), Avenida Menéndez Pidal s/n, 14004 Córdoba, Spain*
[d] *Department of Geography, Swansea University, SA2 8PP Swansea, United Kingdom*

ARTICLE INFO

Editor: Jing M. Chen

Keywords:
Solar-induced chlorophyll fluorescence
SIF
Plant phenotyping
Stress detection
Airborne
Hyperspectral
Hyperspectral imager

ABSTRACT

Solar-induced chlorophyll fluorescence (SIF) can be used as an indicator of crop photosynthetic activity and a proxy for vegetation stress in plant phenotyping and precision agriculture applications. SIF quantification is sensitive to the spectral resolution (SR), and its accurate retrieval requires sensors with sub-nanometer resolutions. However, for accurate SIF quantification from imaging sensors onboard airborne platforms, sub-nanometer imagers are costly and more difficult to operate than the commonly available narrow-band imagers (i.e., 4- to 6-nm bandwidths), which can also be installed on drones and lightweight aircraft. Although a few theoretical and experimental studies have evaluated narrow-band spectra for SIF quantification, there is a lack of research focused on comparing the effects of the SR on SIF from airborne hyperspectral imagers in practical applications. This study investigates the effects of SR and sensor altitude on SIF accuracy, comparing SIF quantified at the 760-nm O_2-A band (SIF_{760}) from two hyperspectral imagers with different spectral configurations (full width at half-maximum resolutions of 0.1–0.2 nm and 5.8 nm) flown in tandem on board an aircraft. SIF_{760} retrievals were compared from two different wheat and maize phenotyping trials grown under different nitrogen fertilizer application rates over the 2019–2021 growing seasons. SIF_{760} from the two sensors were correlated (R^2 = 0.77–0.9, $p < 0.01$), with the narrow-band imager producing larger SIF_{760} estimates than the sub-nanometer imager (root mean square error (RMSE) 3.28–4.69 mW/m^2/nm/sr). Ground-level SIF_{760} showed strong relationships with both sub-nanometer ($R^2 = 0.90$, $p < 0.001$, RMSE = 0.07 mW/m^2/nm/sr) and narrow-band ($R^2 = 0.88$, $p < 0.001$, RMSE = 3.26 mW/m^2/nm/sr) airborne retrievals. Simulation-based assessments of SIF_{760} for SRs ranging from 1 to 5.8 nm using the SCOPE model were consistent with experimental results showing significant relationships among SIF_{760} quantified at different SRs. Predictive algorithms of leaf nitrogen concentration using SIF_{760} from either the narrow-band or sub-nanometer sensor yielded similar performance, supporting the use of narrow-band resolution imagery for assessing the spatial variability of SIF in plant phenotyping, vegetation stress detection and precision agriculture contexts.

1. Introduction

Solar radiation reaching a plant canopy cannot be fully utilized for photosynthesis, and the resulting excess radiation is partly re-emitted as a weak electromagnetic signal termed solar-induced chlorophyll fluorescence (SIF) (see a full review on SIF in Mohammed et al., 2019). SIF flux originates from photosystem II (PSII) and has a spectral range of 650–800 nm with one peak at 685 nm (SIF_{685}) and a second peak at 740 nm (SIF_{740}). The SIF energy dissipation pathway directly competes with the PSII photochemistry and heat dissipation (Krause and Weis, 1984; Lichtenthaler and Rinderle, 1988). Thus, SIF is a proxy for plant photosynthetic rate, which may be related to plant stress levels (Genty

* Corresponding author at: Department of Infrastructure Engineering, Faculty of Engineering and Information Technology (FEIT), University of Melbourne, Melbourne, Victoria, Australia.
E-mail address: pablo.zarco@unimelb.edu.au (P.J. Zarco-Tejada).

https://doi.org/10.1016/j.rse.2022.112986
Received 20 August 2021; Received in revised form 28 February 2022; Accepted 2 March 2022

et al., 1989; Weis and Berry, 1987; Zarco-Tejada et al., 2016). However, SIF emitted from the canopy constitutes a small fraction (1–5%) of the total reflected solar radiation, making it difficult to quantify (Meroni et al., 2009).

Specialized algorithms are necessary for decoupling SIF from total reflected solar radiation. These algorithms are classified based on whether SIF is retrieved within specific absorption bands or over the whole SIF emission region (Mohammed et al., 2019). Most methods utilize discrete solar or telluric absorption lines of the solar spectrum, where the contribution of SIF to the total radiance signal is relatively higher. The terrestrial oxygen absorption bands (O_2-A and O_2-B) centred around 760 nm and 687 nm, respectively, are broader and deeper than the other absorption features and, therefore, commonly used for quantifying SIF (Meroni et al., 2009). The fluorescence *in-filling* method, based on the Fraunhofer Line Depth (FLD) principle (Plascyk, 1975), depends on a few discrete spectral bands inside and outside the oxygen absorption features and is the most widely used method for SIF retrieval due to its ease of implementation. By contrast, spectral fitting methods (SFMs) model the fluorescence and reflectance spectrum by spectral curve fitting, utilizing all the contiguous wavelengths within a fixed spectral window mostly centred around oxygen absorption bands (Meroni et al., 2010; Meroni and Colombo, 2006).

The earliest attempt to incorporate leaf fluorescence into a radiative transfer model (RTM) was the Fluorescence–Reflectance–Transmittance (FRT) model (Zarco-Tejada et al., 2000a, 2000b). This attempt led to the development of the leaf model FluorMODleaf (Pedrós et al., 2008) and a canopy-level RTM named FluorSAIL (Verhoef, 2004). These models prompted the development of an integrated, vertical, one-dimensional, leaf-canopy fluorescence–temperature–photosynthesis model named Soil-Canopy-Observation of Photosynthesis and Energy fluxes (SCOPE) (Van der Tol et al., 2009), which is widely used to assess the linkage between fluorescence–reflectance and photosynthesis (Camino et al., 2019; Celesti et al., 2018; Verhoef et al., 2018). SCOPE simulates top-of-canopy radiance, chlorophyll fluorescence and reflectance for homogenous canopies. It has been used to quantify the effects of the leaf biochemistry, maximum carboxylation rate (Vcmax), and canopy structure on apparent reflectance, including fluorescence effects. Recently, three-dimensional canopy RTMs integrating fluorescence have been developed, such as FluorFLIGHT (Hernández-Clemente et al., 2017), the Fluorescence model with Weight Photon Spread (FluorWPS) (Zhao et al., 2016), and the Discrete Anisotropic Radiative Transfer (DART) model (Gastellu-Etchegorry et al., 2017). These models simulate scattering within the canopy components and thus account for canopy structural heterogeneity.

The earliest experiments involving ground-based sub-nanometer-resolution spectrometers quantified SIF at both leaf (Meroni and Colombo, 2006) and canopy levels (Pérez-Priego et al., 2005), detecting herbicide- and water-induced stress, respectively. The development of sub-nanometer-resolution hyperspectral sensors in the past decade has enabled SIF retrievals from airborne platforms. Sensors include the Chlorophyll Fluorescence Imaging Spectrometer (CFIS) (Frankenberg et al., 2018), the high-resolution airborne imaging spectrometer HyPlant (Rascher et al., 2015), and the Hyperspec High-Resolution Chlorophyll Fluorescence Sensor (Headwall Photonics, Fitchburg, MA, USA) (Belwalkar et al., 2021) with spectral resolutions (SRs) of 0.1, 0.28 and 0.1–0.2 nm, respectively. Sub-nanometer-resolution SIF observations at the global scale are available from satellite sensors such as OCO-2 (Orbiting Carbon Observatory-2) (Frankenberg et al., 2014), GOSAT (Greenhouse gases Observing SATellite) (Guanter et al., 2012), and TROPOMI (TROPOspheric Monitoring Instrument) (Guanter et al., 2015) with spatial resolutions of 1.29 km × 2.25 km, 50 km × 50 km and 5.5 km × 3.5 km, respectively. The European Space Agency is also set to launch the FLuorescence EXplorer (FLEX) (Drusch et al., 2017) in 2024, a mission solely dedicated to measuring SIF at a high SR of 0.3 nm across the globe at 300-m spatial resolution.

As a result of these technical and methodological advances, SIF is frequently used for monitoring crop photosynthesis. SIF is measured from a variety of platforms, including ground-based spectrometers (Cogliati et al., 2015; Daumard et al., 2012; Grossmann et al., 2018; Kim et al., 2021; Li et al., 2020; Pérez-Priego et al., 2005; Rossini et al., 2016), drones and manned aircraft (Bandopadhyay et al., 2019; Damm et al., 2014, 2015; Siegmann et al., 2019; Tagliabue et al., 2020; Zarco-Tejada et al., 2012, 2013a) and satellite platforms (Frankenberg et al., 2014; Guanter et al., 2012, 2015). SIF observations at intermediate scales obtained from airborne platforms are important for i) improving the interpretation of SIF at coarser spatial resolutions and thus bridging the gap between field and global scales, ii) disentangling the contribution of different scene components in aggregated pixels (Hornero et al., 2021a; Zarco-Tejada et al., 2013b), and iii) evaluating the sensitivity of SIF for describing plant physiological processes at high spatial resolutions (e.g., as an early indicator of biotic and abiotic stress in precision agriculture and forestry).

Modelling studies (Damm et al., 2011; Liu et al., 2015) of FLD-based SIF retrieval have shown that sensor SR and the signal-to-noise ratio (SNR) (collectively accounting for more than 80% of the retrieval error) strongly affect SIF measurement accuracy. Several studies have demonstrated the potential of sub-nanometer airborne hyperspectral imagers for precise SIF quantification in a variety of contexts, including estimating gross primary productivity (GPP) (Wieneke et al., 2016), validating satellite-based SIF retrievals (Sun et al., 2017), assessing the physiological effects of age on loblolly pine forest (Colombo et al., 2018) and quantifying functional diversity of terrestrial ecosystems (Tagliabue et al., 2020). Although sub-nanometer-resolution imaging sensors are recommended for obtaining absolute measurements of SIF, relative SIF measurements from narrow-band sensors are useful in a variety of settings, including water stress detection (Camino et al., 2018a; Panigada et al., 2014; Zarco-Tejada et al., 2012), plant phenotyping (Camino et al., 2019, 2018b; Gonzalez-Dugo et al., 2015), biotic-induced stress detection (Calderón et al., 2015, 2013; Hernández-Clemente et al., 2017; Hornero et al., 2021b; Poblete et al., 2020, 2021; Zarco-Tejada et al., 2018) and linking canopy-level SIF_{760} and GPP using sensors such as the Airborne Prism Experiment (APEX) with a full width at half-maximum resolution (FWHM) of 5.7 nm over perennial grassland, cropland and mixed temperate forest (Damm et al., 2015). In these studies, the reported higher levels of the quantified SIF_{760} were consistent with other modelling and experimental studies (Julitta et al., 2016; Nakashima et al., 2021; Nichol et al., 2019; Süß et al., 2016).

The impacts of SR on FLD-based SIF retrievals have been previously assessed with models (Damm et al., 2011; Dechant et al., 2017; Hernández-Clemente et al., 2017; Liu et al., 2015) and experiments (Julitta et al., 2016). Julitta et al. (2016) compared SIF retrievals at both the O_2-A and O_2-B bands using four portable field spectrometers with different spectral sampling intervals (SSIs), SRs, and SNRs simultaneously measuring the same vegetation target. SIF estimates at the O_2-A band from three of the four spectrometers with sub-nanometer resolution (FWHM $\leq$1 nm) were consistent with the expected ranges from ground-based SIF observations over lawn grassland reported by Rossini et al. (2016). In contrast, the average SIF from the coarsest-resolution spectrometer (FWHM = 5.5 nm) was six times higher than the values obtained from the other three spectrometers, reaching values above 4 $mW/m^2/nm/sr$. Our study expands on this previous work by assessing the effects of SR and flight altitude on airborne-based SIF retrievals, which are commonly used in precision agriculture applications. This is, to the best of our knowledge, the first study to do so. Aspects regarding the effects of the atmosphere, flight altitude, and performance of imaging sensors on SIF retrievals need to be studied in addition to the theoretical work and the assessments carried out using close-range spectrometer data.

The need for sub-nanometer imagers for the accurate quantification of SIF brings important challenges in precision agriculture, plant phenotyping and biosecurity applications due to their complexity, higher cost and increased operational difficulties. Standard narrow-band hyperspectral imagers (i.e., with SR in the range of 4–6 nm FWHM) are an appealing alternative that are increasingly being used with drones and lightweight aircraft to collect high-spatial-resolution imagery (Aasen et al., 2018). However, it is unclear how useful SIF_{760} estimates from these imagers are for plant physiological assessments when compared to ground-based or sub-nanometer airborne SIF_{760} estimates. Such assessment is critical, particularly when the relative quantification of fluorescence across the landscape could be readily used to detect biotic- and abiotic-induced vegetation stress. Empirical work is needed to evaluate whether SIF_{760} retrievals from these narrow-band hyperspectral imagers are sufficient for detecting physiological stress in crops, relative to measurements from sub-nanometer instruments.

Monitoring crop nutrient status is one potentially important application of airborne SIF_{760} quantification (Camino et al., 2018b; Wang et al., 2021). Accurate assessments of plant nutrition across a field can help to ensure crop yields by allowing for more efficient use of N-fertilizers. Excessive N fertilizer application can result in the loss of reactive forms of N (ammonia, nitrate, and nitrogen oxides) to the environment, causing water pollution, climate forcing, and biodiversity loss. As a result, assessing crop response to N-fertilizers is critical for ensuring resource efficiency while optimizing yields.

In this study, we compared SIF_{760} measured from a 5.8-nm FWHM narrow-band hyperspectral imager to a sub-nanometer hyperspectral imager of 0.1- to 0.2-nm FWHM flown in tandem at multiple sensor altitudes and across two wheat and maize trials grown under different nitrogen application rates and for three growing seasons. We validated airborne measures with sub-nanometer ground retrievals and evaluated results against SCOPE simulations. We then assessed the performance of sub-nanometer and narrow-band SIF_{760} estimates for predicting nitrogen concentration using machine learning models. Our findings provide important insights that support the operational use of standard, commercially available narrow-band hyperspectral imagers for

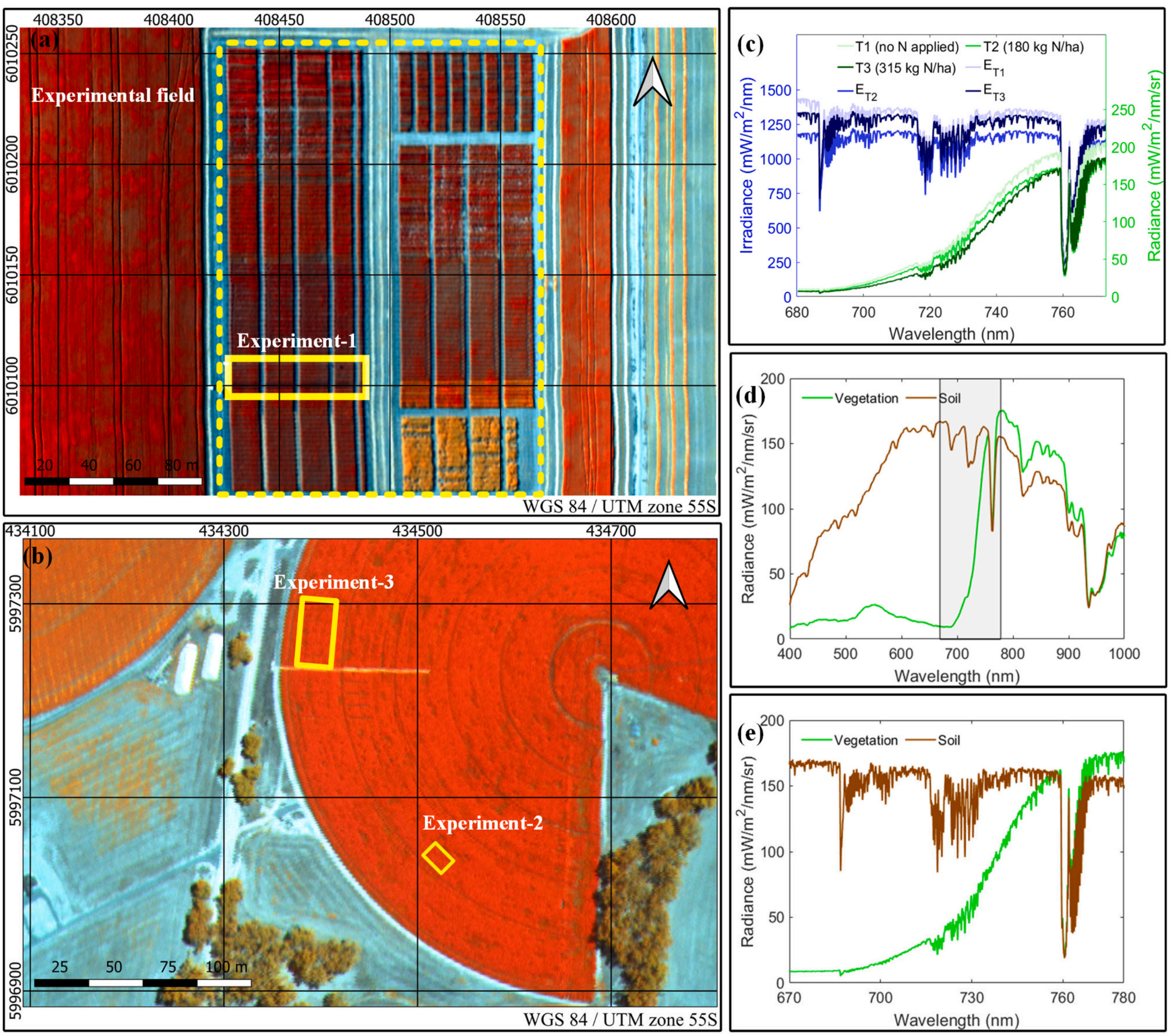

Fig. 1. Overview of experiments at field trial sites 1 (a) and 2 (b). Sample average radiance and the corresponding irradiance (E) spectra for experimental plots subjected to different nitrogen treatments at experiment 3 obtained from HR-2000 (c). Sample radiance spectra acquired from the narrow-band hyperspectral imager (d) and sub-nanometer hyperspectral imager (e) corresponding to the same vegetation and soil targets. (a) was acquired with the narrow-band hyperspectral imager (composite: 760 (R), 710 (G) and 680 (B) nm). (b) was obtained with the sub-nanometer hyperspectral imager (composite: 760 (R), 710 (G) and 680 (B) nm). The solid yellow boxes in (a) and (b) show the location of the plots across the three experiments and the dashed yellow box in (a) shows the location of plots across the entire field. The transparent grey box in (d) shows the spectral region covered by the sub-nanometer hyperspectral imager. (For interpretation of the references to colour in this figure legend, the reader is referred to the web version of this article.)

quantifying relative SIF levels. This is especially important for precision agriculture and plant physiology monitoring purposes that require accurate assessment of the SIF variability within and across experimental fields.

2. Materials and methods

2.1. Study sites and field data collection

Experiments took place at two field trial sites in Victoria, Australia, in 2019, 2020 and 2021 (Fig. 1a and b). Experiment 1 was conducted over 15 plots of dryland wheat (cv. Scepter) (Yang et al., 2018) located at site 1 in Yarrawonga (36°02′55″S, 145°59′02″E). Plots were 26 m^2 (2 m × 13 m) and planted in May 2019. Plots were grown with five different rates of nitrogen fertilizer in the form of urea (46% N) (T1: 0 kg N/ha, T2: 46 kg N/ha, T3: 92 kg N/ha, T4: 138 kg N/ha, T5: 184 kg N/ha). The surrounding areas were planted with several varieties of wheat grown under various physiological conditions and nitrogen fertilizer application rates (Fig. 1a).

Experiments 2 and 3 were conducted in 2020 and 2021 at site 2 in Peechelba East (36°10′04″S, 146°16′23″E) over irrigated maize plots. Experiment 2 consisted of 8 plots and experiment 3 consisted of 20 plots. Plots were sown in October 2019 and October 2020 with two urea application rates for experiment 2 (T1: 207 kg N/ha, T2: 387 kg N/ha) and three for experiment 3 (T1: 0 kg N/ha, T2: 180 kg N/ha, T3: 315 kg N/ha). The plot sizes were 15 m^2 (3 m × 5 m) for experiment 2 and 36 m^2 (3 m × 12 m) for experiment 3. The climate at both field trial sites is humid subtropical (Cfa) according to the Köppen classification. At site 1, the mean annual temperature is 16.3 °C and average rainfall is 559 mm. At site 2, the mean annual temperature is 15.2 °C and average rainfall is 642 mm.

For experiment-3, field measurements of top-of-canopy (TOC) spectral radiances for the computation of ground-based SIF_{760} were collected from all 20 plots on 20 January 2021 at midday from 11:45 to 16:30 solar time under clear sky conditions. TOC spectral radiance was measured using a 0.065-nm FWHM HR-2000 spectrometer (Ocean Insight, Dunedin, FL, USA). The total incoming irradiance was calculated using the radiance reflected from a white reference panel (Labsphere Inc., North Sutton, NH, USA) measured by the spectrometer. The spectral measurements were acquired from the nadir using bare optical fiber, with an angular field of view of 25°, mounted on a tripod of 2.5 m height. The vegetation targets were measured at a distance of 1 m above the canopy. Radiance measurements were recorded at five different locations within each plot and then averaged to reduce noise. Incident solar radiation was measured prior to radiance measurements, and radiance/irradiance measurements were completed within 3 min for each plot. Examples of radiance and irradiance measurements are shown in Fig. 1c, with visible differences in spectra associated with applied nitrogen rate.

A summary of the physiological measurements performed at each experiment is shown in Table 1. The growth stages during the airborne campaigns corresponded to i) grain filling (milking stage) for wheat in 2019, ii) dough stage for maize in 2020, and iii) silking stage for maize in 2021. A portable weather station (model WXT510, Vaisala, Helsinki, Finland) was installed in the field for concurrent readings of meteorological conditions at the time of hyperspectral image acquisitions. For experiments 1 and 3, leaf measurements were carried out under field conditions, coincident with the airborne campaigns. For experiment 2, leaf measurements were performed 4 days prior to the airborne campaign under similar meteorological conditions (Table 1). Measurements were made on 10–15 leaves per plot for experiment 1 and 5–10 leaves per plot for experiments 2 and 3. Measurements were made on leaves at the top of the canopy at noon, under clear skies. Chlorophyll content, nitrogen balance index (NBI), flavonols and anthocyanin content were measured using a handheld Dualex leaf-clip sensor (FORCE-A, Orsay, France). Steady-state leaf fluorescence yield (Ft) was measured using the FluorPen FP110-LM (Photon Systems Instruments, Drásov, Czech Republic) handheld fluorometer. Random samples of 10–15 leaves per plot for experiment 1 and 4–5 leaves per plot for experiments 2 and 3 from the top of the canopy were selected for determining the total N concentration (%) destructively in the laboratory, following the Kjeldahl method (Kjeldahl, 1883). To verify the impacts of fertilization rate on leaf physiological traits, measurements were evaluated using analysis of variance (ANOVA) followed by a Dunnett's test at $\alpha < 0.05$. In addition to the 15 plots at site 1, leaf-level measurements from more than 100 adjacent plots within the entire experimental field (dashed yellow box in Fig. 1a) were also conducted to investigate the intra-field variability.

2.2. Airborne hyperspectral campaigns

Airborne campaigns were conducted in 2019, 2020 and 2021 (Table 2), flying with the aircraft's heading on the solar plane. Two hyperspectral imagers were installed in tandem on a Cessna-172 aircraft operated by the HyperSens Laboratory, University of Melbourne's Airborne Remote Sensing Facility. The first hyperspectral imager was a Hyperspec VNIR *E*-Series model (Headwall Photonics, Fitchburg, MA, USA) and the second hyperspectral imager was a high-resolution Hyperspec Fluorescence sensor (Headwall Photonics, Fitchburg, MA, USA). The spectral characteristics of both hyperspectral imagers are shown in Table 3. Both hyperspectral imagers were radiometrically calibrated in the laboratory using an integrating sphere (Labsphere XTH2000C, Labsphere Inc., North Sutton, NH, USA); as a result, coefficients derived from the constant light source at four different illumination levels were calculated for the flight configuration of each imager. The atmospheric correction for the VNIR imager was performed using the SMARTS model (Gueymard, 2001), with the aerosol optical depth measured at 550 nm with a Microtops II sunphotometer (Solar LIGHT Co., Philadelphia, PA, USA), allowing the conversion of the radiance values to reflectance. Image orthorectification was conducted with PARGE (ReSe Applications Schläpfer, Wil, Switzerland) using inputs from the solidly installed and synchronized inertial measurement units (VN-300-VectorNav Technologies LLC, Dallas, TX, USA for VNIR imager and Trimble APX-15 UAV, Applanix Corporation, Ontario, Canada for Fluorescence imager); more information on data pre-processing and image correction can be found in Zarco-Tejada et al. (2016).

Differences in radiance spectra corresponding to vegetation and soil targets acquired from the two hyperspectral imagers were visually identified as a function of spectral configurations (Fig. 1d and e). Above-ground-level (AGL) altitudes and spatial resolutions of the imagery are detailed in Table 2. The spatial resolution of imagery from both airborne hyperspectral imagers was sufficient for identification of individual plots over the experimental sites (Fig. 2). Differences in fertilization rate could be visually discriminated based on radiance spectra acquired from both the hyperspectral imagers over the entire spectral range (Fig. 3a and c) and in the O_2-A absorption feature (Fig. 3b and d) for experiment 1.

To investigate the impact of sensor altitude on the inter-comparison of airborne-quantified SIF_{760} from both hyperspectral imagers and with ground-based SIF_{760}, images from both hyperspectral imagers were acquired at three different altitudes (900 m, 1200 m and 2200 m) for experiment 3 (Table 2). All images were acquired within a 20-min time interval to minimize the impact of sun-sensor geometry and changes in atmospheric conditions on the SIF_{760} retrievals. The effect of sensor height on O_2-A absorption feature depth and SIF_{760} quantifications was assessed using ANOVA followed by Tukey's honest significant difference (HSD) post-hoc test at $\alpha < 0.05$. Fig. 4 shows the impact of the sensor altitude on the radiance spectra for the sub-nanometer imager. The radiance imagery acquired from the sub-nanometer imager at three different altitudes over the entire field (Fig. 4a, b and c) and over the experimental plots (Fig. 4d, e and f) differed in the 670- to 780-nm

Table 1
Field measurements and meteorological conditions coincident with flights.

Field trial site	Experiment #	Treatment (kg N/ha)	Growth stage	Field measurements	Meteorological conditions		
					T_a	RH	P_a
Yarrawonga (Site 1)	1	T1:0, T2:46, T3:92, T4:138, T5:184	Grain filling	Ft, Chl, NBI, Flav, Anth, TN	19.2	30.1	1002.8
Peechelba (Site 2)	2	T1:207, T2:387	Dough	Ft, Chl, NBI, Flav, Anth, TN	23.3	36.2	1008.5
	3	T1:0, T2:180, T3:315	Silking	Ft, Chl, NBI, Flav, Anth, TN, TOC L	25.3	33.5	1003.6

Ft = Steady-state chlorophyll fluorescence, Chl = Chlorophyll content (μg/cm^2),
NBI = Nitrogen balanced index (Dualex unit (d.u)), Flav = Flavonols (Dualex unit),
Anth = Anthocyanins (Dualex unit), TN = Total Nitrogen concentration (%),
TOC L = Top-of-canopy radiance (mW/m^2/nm/sr) from HR-2000, T_a = Average air temperature (°C),
RH = Relative humidity (%) and P_a = Average air pressure (mBar).

Table 2
Flight dates, flight altitudes and spatial resolution of the acquired hyperspectral images during the three airborne campaigns.

Flight date	Flight time (local)	Experiment	AGL (m)		Spatial resolution (m)	
			NB	SN	NB	SN
09/10/19	15:40–16:30	1	400	900	0.25	0.20
16/03/20	12:50–13:50	2	700	850	0.50	0.20
20/01/21	11:40–12:20	3	900	900	0.65	0.20
			1200	1200	0.9	0.30
			2200	2200	1.7	0.55

NB = Narrow-band hyperspectral imager.
SN = Sub-nanometer hyperspectral imager.
AGL = above ground level.

Table 3
Spectral characteristics of the airborne hyperspectral imagers.

Configuration	Fluorescence sensor (Sub-nanometer imager)	VNIR *E*-Series sensor (Narrow-band imager)
Spectral range	670–780 nm	400–1000 nm
Number of spectral bands	2160	371
Spectral sampling interval	0.051 nm	1.626 nm
FWHM	0.1–0.2 nm	5.8 nm
Number of un-binned spatial pixels	1600	1600
SNR	>300:1*	>300:1*
Field of view	23.5°	66°
Aperture	f/2.5	f/2.5
Bit depth	16	16

* With spatial binning.

spectral region (Fig. 4g) and in the oxygen absorption features (Fig. 4h and i).

2.3. *SIF quantification from field data and airborne hyperspectral imagery*

A thresholding approach based on the normalized difference vegetation index (NDVI) was used to select the pixels corresponding to vegetation in each individual plot. To ensure that only pure vegetation pixels were considered for the analysis, all pixels with an NDVI greater than 0.6 were selected. For each plot, mean radiance spectra were calculated by averaging spectra from all pure vegetation pixels within the plot, excluding boundary pixels, from hyperspectral images acquired from both imagers. This object-based analysis strategy was used to reduce the uncertainty when using pixel-based SIF retrievals due to the SNR of the instrument. For experiment 1, the total incoming irradiance at the flight time was measured using the HR-2000 spectrometer with a CC-3 VIS-NIR cosine corrector diffuser. Due to the unavailability of cosine corrector diffuser for experiments 2 and 3, the total incoming irradiance at the flight time was calculated by measuring the radiance reflected from the white reference panel by the spectrometer. Ground-based SIF_{760} from eight plots measured concurrently with airborne image acquisition were used to validate the airborne SIF_{760} calculated from both imagers. The relative root mean square error (rRMSE) was calculated between the airborne and ground-based SIF_{760} following Eq. (1):

$$rRMSE = \sqrt{\frac{\sum_{i=1}^{n}\left(\frac{F_{airborne,i}-F_{ground,i}}{F_{ground,i}}\right)^2}{n}} \times 100\% \tag{1}$$

where $F_{airborne,\ i}$ and $F_{ground,\ i}$ are the SIF_{760} values retrieved from airborne and ground-based spectrometers, respectively, for plot *i*, with *n* representing the number of plots.

Field spectrometer radiances/irradiances were calibrated using coefficients derived from a uniform calibrated light source and an integrating sphere (Labsphere XTH2000C). To match the SR of the radiance images acquired from both sensors, the high-resolution irradiance spectra acquired with the HR-2000 spectrometer was resampled through Gaussian convolution (Hornero et al., 2021b; Suarez et al., 2021) corresponding to the SR of the airborne hyperspectral imagers. As the spectral characteristics of the narrow-band hyperspectral imager do not meet the requirements (Drusch et al., 2017; ESA, 2015) for quantifying SIF at the O_2-B (SIF_{687}) absorption feature, SIF_{687} values were not compared. This limitation also affects the applicability of SFMs with the narrow-band hyperspectral imager, as it requires sub-nanometer resolution for accurate SIF quantification. Thus, the retrieval of SIF_{760} using irradiance derived from HR-2000 measurements and average radiance derived from airborne hyperspectral images and ground-based HR-2000 measurements was performed using the O_2-A-band *in-filling* method through the FLD principle, based on a total of three spectral bands (3FLD) (Maier et al., 2003). The spectral window for '*in*' and '*out*' irradiance (E) and radiance (L) used in 3FLD computation was selected based on the spectral characteristics of the measuring instruments. For the narrow-band imager, E_{in}/L_{in} corresponds to the E/L minima in the 755–765 nm region. The minima for both E and L was observed at 762 nm, and this was consistent for all datasets. E_{out}/L_{out} corresponds to the weighted mean of E/L maxima in the spectral regions of 750–755 nm and 771–776 nm, respectively following the methodology proposed in Damm et al. (2011). The spectral window for both ground-based and airborne sub-nanometer sensors was selected using the methodology proposed in Julitta et al. (2017),[1] which considers the FWHM of the sub-nanometer resolution instrument and uses the mean of E/L in the left and right shoulder regions to reduce noise. An additional data quality check was performed for the matching of the '*in*' band for E/L, and in the event of a mismatch, E_{in}/L_{in} was defined as the mean of E_{in}/L_{in} of adjacent wavelengths. The absolute depth (in radiance units) and

[1] R code available on GitHub platform at https://github.com/tommasojulitta

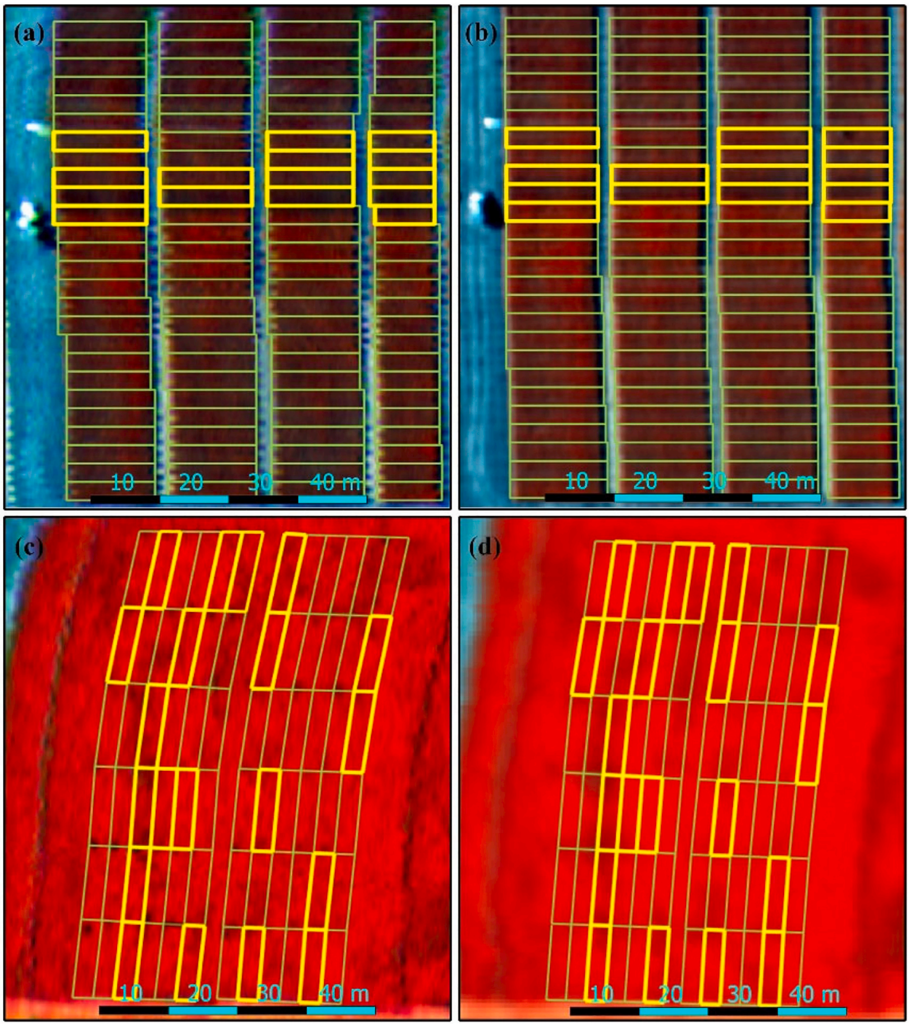

Fig. 2. Hyperspectral imagery showing zoomed-in plots from identical locations in experiments 1 (a, b) and 3 (c, d). Images (a) and (c) were acquired with the sub-nanometer hyperspectral imager (composite: 760 (R), 710 (G) and 680 (B) nm). Images (b) and (d) were acquired with the narrow-band hyperspectral imager (composite: 760 (R), 710 (G) and 680 (B) nm). Green polygons indicate plots under different nitrogen treatments, and yellow polygons indicate the selected plots corresponding to five and three nitrogen treatments, respectively, for experiments 1 and 3. (For interpretation of the references to colour in this figure legend, the reader is referred to the web version of this article.)

relative depth (in percent) of the O_2-A band feature were calculated in addition to the airborne SIF_{760} quantification. The absolute depth was calculated as the difference between the solar radiance at the left shoulder wavelength and the wavelength at the bottom of the O_2-A absorption feature, and the relative depth was calculated as the ratio of absolute depth and the solar radiance at the left shoulder wavelength. The wavelength providing the highest radiance in the 750–759 nm range was selected as the left shoulder wavelength.

In the absence of atmospheric correction, SIF_{760} values could be negative even for fluorescent targets (see Fig. 6 in Marrs et al., 2021). The atmospheric correction process involves estimating several atmospheric parameters such as upwelling transmittance, path scattered radiance, and spherical albedo using atmospheric RTMs. Additionally, to account for uncertainties in the estimation of atmospheric parameters, the transmittance correction technique (Damm et al., 2014; Guanter et al., 2010; Siegmann et al., 2019) is a commonly used approach that forces the non-fluorescent targets to give zero SIF_{760}. Due to the complexities involved in accurately estimating the atmospheric parameters, RTM-based atmospheric correction was not performed in the current study. Instead, on account of the successful implementation of a rescaling scheme to correct negative airborne SIF_{760} and SIF_{687} values in Bandopadhyay et al. (2019), we used a simplified correction technique based on the same principle of using non-fluorescent targets (i.e., bare soil) as in the widely used transmittance correction technique, to compensate for negative SIF_{760} values related to calibration and atmospheric factors such as aerosol scattering and surface pressure. Any deviation from the non-fluorescent behaviour of bare soil targets identified in each image was attributed to spectral miscalibration or atmospheric effects. The method relies on forcing the non-fluorescent target to give zero SIF_{760}, and the non-zero SIF_{760} served as an offset to correct the SIF_{760} from vegetation targets following Eq. (2):

$$SIF_{corrected} = SIF_{vegetation\ target} - SIF_{non-fluorescent\ target} \tag{2}$$

To minimize the directional effects on the airborne-quantified SIF_{760}, the corrected SIF_{760} was normalized to a reference-viewing angle using a reflectance-based angular correction approach (Hao et al., 2021). The normalization method employs a reference SIF_{760} corresponding to a reference viewing angle, as well as near-infrared reflectance of vegetation (NIRv) (Badgley et al., 2017), to normalize SIF_{760} quantified at any viewing direction to a reference viewing angle. Two different approaches were used to compute the reference SIF_{760} for normalization. In the first approach, a single plot located at the centre of each hyperspectral image was selected as the reference SIF_{760} on account of being a nadir-view. In the second approach, locations of the ground-based spectral measurements were identified in the hyperspectral images and used for calculating the reference SIF_{760}. Since the ground-based spectral measurements were primarily conducted along the plot's centre, only pure vegetation pixels located along the plot's centre were used to compute mean radiance for the reference SIF_{760} calculation. This differs from the airborne SIF_{760} corresponding to individual plots, which was calculated using mean radiance from all pure vegetation pixels excluding the boundaries. The second approach was only applied for

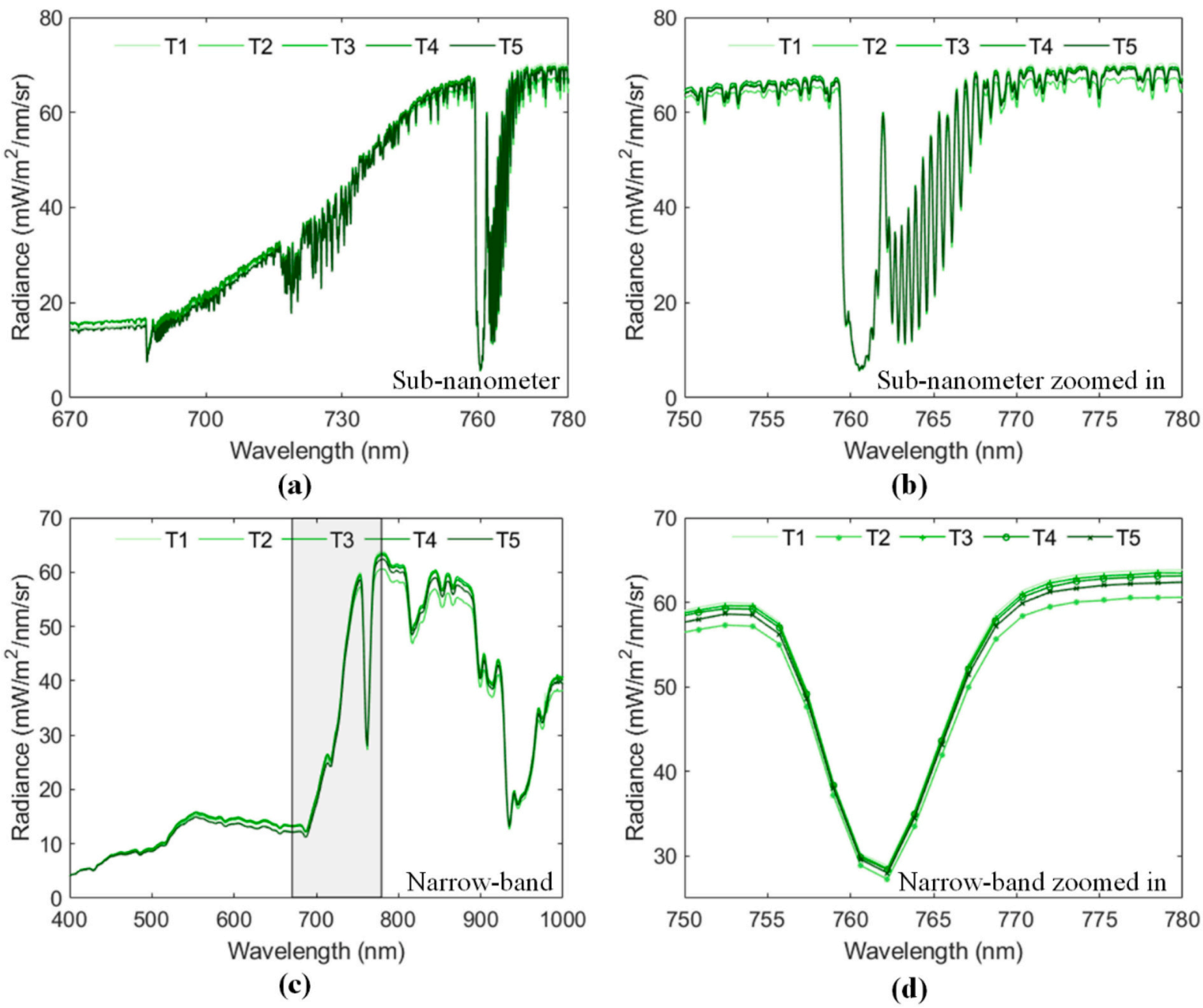

Fig. 3. Average radiance spectra for treated plots in experiment 1. Spectra obtained from (a) the sub-nanometer imager in the 670- to 780-nm region, (b) the sub-nanometer imager in the O_2-A absorption region, (c) the narrow-band imager in the 400- to 1000-nm region and (d) the narrow-band imager in the O_2-A absorption region. The transparent grey box in (c) shows the spectral region covered by the sub-nanometer hyperspectral imager. Codes T1-T5 correspond to the applied nitrogen fertilization rates shown in Table-1.

experiment 3 to validate the airborne-quantified SIF_{760} with the ground-based HR-2000 SIF_{760} measurements so that the reference viewing direction remained identical for ground-based and airborne SIF_{760}. Normalization was conducted according to the nadir-viewing angle for all inter-comparisons of airborne SIF_{760} from both imagers.

The study focused on assessing the spectral configuration of the two instruments, with attempts made to reduce distortions caused by other factors. We used pixels close to the nadir-viewing angle and avoided evaluating areas close to the image borders to reduce the potential effects of instrument 'smile' on assessment of the two instruments. Moreover, the angular correction used to normalize SIF_{760} minimizes the potential instrument smile effects (detailed above). Further work and a corresponding paper will evaluate sensor smile effects and corrections needed when using narrow-band instruments for SIF_{760} retrievals. This additional work is important because entire images, rather than just nadir pixels, are needed for practical applications in precision agriculture.

2.4. Modelling the spectral resolution effects on SIF quantification using SCOPE simulations

The SCOPE model integrates three radiative transfer modules and an energy balance module to estimate outgoing radiation spectra, turbulent heat fluxes, photosynthesis rates and chlorophyll fluorescence (Van der Tol et al., 2009). Surface reflectance and fluorescence spectra are simulated by linking several energy balance, photosynthesis and canopy biophysical parameters with TOC radiance, with SSI and SR of 1.0 nm each. The model assumes a homogenous canopy structure, and the canopy radiative transfer equations are based on the widely used SAIL model (Verhoef, 1984). Net radiation over the canopy is calculated by integrating the contribution from the individual layers with shaded and sunlit leaves at different leaf angles over the canopy depth. The canopy reflectance modelling is conducted based on four different Bidirectional Reflectance Distribution Function (BRDF) terms representing direct and diffused hemispherical contribution from the surrounding and the direct and diffused reflectance in the viewing direction. The leaf-level fluorescence spectra are modelled within the 640- to 850-nm spectral region based on the FLUSPECT model (Vilfan et al., 2016) by utilizing the leaf reflectance and fluorescence outputs derived from the PROSPECT model (Jacquemoud and Baret, 1990).

A simulated dataset using the SCOPE model (version 2.0) was generated to evaluate the influence of the SR of the airborne hyperspectral sensors on the 3FLD-based SIF_{760} quantification. The dataset consisted of 400,000 simulations generated by randomly varying specific input parameters, drawing from a uniform distribution within ranges shown in Table 4. All other SCOPE input parameters were kept at their default values. The air temperature and air pressure inputs for the SCOPE model were measured with a portable weather station during the

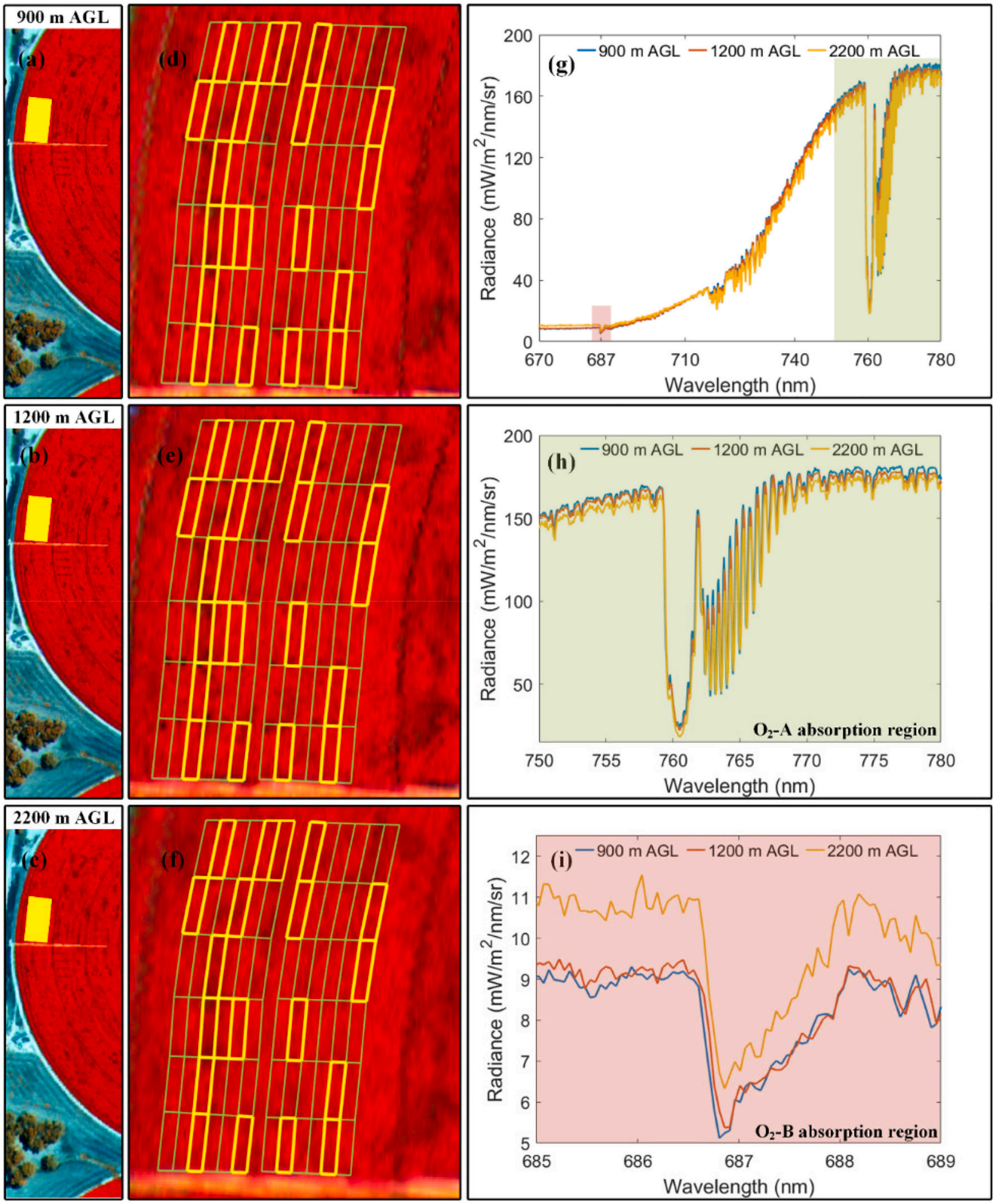

Fig. 4. Hyperspectral imagery from experiment 3. (a–f) Sub-nanometer composite imagery (760 (R), 710 (G) and 680 (B) nm) at various altitudes. (g–i) Average radiance spectra acquired for one of the experimental plots in the 670- to 780-nm region (g), O_2-A absorption region (h) and O_2-B absorption region (i). Area of yellow filled polygons (a, b, c) shown in detail in (d), (e) and (f), respectively. Green polygons indicate plots under different nitrogen treatments, and yellow polygons indicate the selected plots corresponding to three nitrogen treatments. (For interpretation of the references to colour in this figure legend, the reader is referred to the web version of this article.)

airborne campaign at field trial site 1. Details regarding the definition and ranges of all input parameters can be found in Supplementary Data S1. For each case, the TOC spectra of total upwelling radiance, SIF radiance and the corresponding irradiance were simulated using the default 1.0-nm SR and 1.0-nm SSI obtained from SCOPE. To compare the SIF_{760} retrieval performance for SR corresponding to the narrow-band hyperspectral imager, SCOPE-simulated spectra were resampled to 5.8-nm FWHM through Gaussian convolution matching the SSI with the narrow-band imager. The resampled radiance spectra in the 400- to 1000-nm spectral region were compared with the average radiance spectra obtained from the narrow-band imager at experimental field trial site 1 using RMSE as the cost function. For each narrow-band airborne radiance spectrum, we selected the 10 closest resampled radiance spectra from the 400,000 simulations along with their corresponding resampled-irradiance for the analysis. Fig. 5a shows the measured radiance spectra from the narrow-band imager. Fig. 5b and c show the SCOPE-simulated SIF and radiance spectra at 1-nm FWHM corresponding to the selected simulations. A comparison of the simulated SCOPE radiance spectra against the narrow-band imager is shown in Fig. 5d. Additionally, radiance and irradiance spectra corresponding

Table 4
Range of the SCOPE input parameters used in this study.

Parameter	Range/ Value	Unit	Description
C_{ab}	10–50	$\mu g \cdot cm^{-2}$	Chlorophyll $a+b$ content
C_{dm}	0.001–0.05	$g \cdot m^{-2}$	Dry matter content
C_w	0.001–0.05	cm	Leaf water equivalent layer
N	1.2–1.8	–	Leaf thickness parameters
Vcmax	20–120	$\mu mol \cdot m^{-1} \cdot s^{-1}$	Maximum carboxylation capacity at 25 °C
fqe	0.001–0.015	–	Fluorescence quantum yield efficiency at photosystem level
LAI	2–6	$m^2 \cdot m^{-2}$	Leaf area index
$LIDF_a$	−1–0	–	Leaf inclination
$LIDF_b$	0	–	Variation in leaf inclination
R_{in}	600–1000	$W \cdot m^{-2}$	Broadband incoming shortwave radiation
Ta	19.2	°C	Air temperature
p	1002.8	hPa	Air pressure
tts	35.42	deg.	Solar zenith angle

to SRs of 2.0 nm, 3.0 nm, 4.0 nm and 5.0 nm were generated by resampling SCOPE-simulated 1.0-nm SR spectra with Gaussian convolution but keeping the SSI at 1.0-nm. Fig. 5e and f show the comparison between the radiance spectra simulated by SCOPE at different SRs in the O_2-B and O_2-A absorption regions, respectively. The O_2-B absorption feature could only be identified at the default 1.0-nm SR. The decrease of SR from the default 1 nm to 5.8 nm resulted in O_2-A-band depth reduction and an increment in the radiance signal corresponding to the absorption minima.

2.5. Nitrogen assessments using narrow-band and sub-nanometer SIF retrievals

The effects of sensor SR on nitrogen estimation was assessed using models with chlorophyll content and SIF traits as inputs (Camino et al., 2018b). Nitrogen content was predicted using Random Forest (RF) (Breiman, 2001) models fit to data from field trial site 1, using i) C_{ab} derived from the narrow-band hyperspectral imagery through the inversion of PRO4SAIL RTM and ii) SIF_{760} quantified from each of the hyperspectral imagers as inputs. The PRO4SAIL model used coupled PROSPECT-D (Féret et al., 2021) and 4SAIL (Verhoef et al., 2007) to retrieve the biochemical constituents and canopy structural parameters, respectively. A look-up table with 200,000 simulations was built by randomly varying the biochemical and biophysical parameters with a uniform distribution within the ranges shown in Table 5.

Support vector machines (SVMs) were trained using simulated reflectance as inputs. Reflectance spectra were matched with the spectral resolution of the narrow-band hyperspectral imager (5.8-nm FWHM). SVMs were first trained in parallel (MATLAB parallel computing toolbox) using a radial basis function and optimizing the hyperparameters during training to predict $C_{ab.}$ Then, using the average reflectance spectra extracted from pure-vegetation pixels, C_{ab} was estimated for each experimental plot. Subsequently, RF regression models were fit for each hyperspectral sensor, using crop N concentration as a response variable and the estimated C_{ab} from the narrow-band VNIR reflectance spectra ($C_{ab\text{-}narrow}$) and SIF_{760} derived from each hyperspectral imager (i.e., $C_{ab\text{-}narrow} + SIF_{760\text{-}narrow}$ vs. $C_{ab\text{-}narrow} + SIF_{760\text{-}sub\text{-}nanometer}$) as predictors.

3. Results

In experiment 1, leaf physiological traits were significantly different in plots fertilized at different rates ($p < 0.05$; Fig. 6). For experiments 2 and 3, differences were non-significant, but there was visible variation in leaf physiological variables among plots receiving different nitrogen treatments (Fig. 6). Differences in leaf total N concentration measured by destructive sampling were generally consistent with the trends observed in leaf steady-state fluorescence (Ft) with minor exceptions (e.g., values observed for T3 in experiment 1). Ft was lower in plots with the least N applied compared to other plots in all the experiments (Fig. 6, Ft and Total N panels). Fertilization rate was positively associated with chlorophyll $a+b$ content and the leaf nitrogen balance index (NBI), while leaf flavonols and anthocyanins were inversely associated with fertilization rate. Leaf physiological values were more variable in experiment 1 (T1–T5: 0–184 kg N/ha) than in experiments 2 (T1–T2: 207–387 kg N/ha) or 3 (T1–T3: 0–315 kg N/ha).

The absorption features at O_2-A and O_2-B absorption regions were evident in the radiance spectra from both airborne hyperspectral imagers (Fig. 7). However, their shape and depth were strongly influenced by the SR. As a result of the coarser SR of the narrow-band imager, the absorption feature at the O_2-B band in the 685- to 690-nm spectral region could not be identified in the narrow-band radiance spectra (Fig. 7, inset). This result restricts the comparison between the narrow-band and sub-nanometer hyperspectral imagers for the calculation of SIF at the O_2-B band. Moreover, a reduction in the depth of the O_2-A absorption feature in the 750- to 780-nm spectral region and the corresponding increment in the radiance signal at the absorption minima were observed for the narrow-band radiance spectra, as expected (Fig. 7, inset). The wavelength corresponding to the radiance minimum was shifted towards higher wavelengths when compared to sub-nanometer radiance spectra, as shown in several studies (Cendrero-Mateo et al., 2019; Damm et al., 2011; Julitta et al., 2016; Liu et al., 2015).

At site 1, the depths of the O_2-A absorption feature from each of the two imagers were strongly correlated ($R^2 = 0.90$, $p < 0.001$; Fig. 8a), when using data from the full set of >100 plots. Nevertheless, the range of SIF_{760} values quantified with the 3FLD method ($SIF_{760\text{-}3FLD}$) differed between sub-nanometer imager (0.05–1.95 $mW/m^2/nm/sr$) and the narrow-band imager (0.37–8.12 $mW/m^2/nm/sr$; Fig. 8b). Although there was some lack of correspondence in $SIF_{760\text{-}3FLD}$ between the two imagers (RMSE = 3.86 $mW/m^2/nm/sr$), the two were significantly correlated ($R^2 = 0.85$, $p < 0.001$; Fig. 8b).

Airborne $SIF_{760\text{-}3FLD}$ estimates from both hyperspectral imagers are compared in Fig. 9. The best agreement between measures was observed in experiment 3 ($R^2 = 0.9$, RMSE = 3.28 $mW/m^2/nm/sr$, $p < 0.001$). Measures from each sensor were also well correlated in experiments 1 ($R^2 = 0.87$, RMSE = 4.69 $mW/m^2/nm/sr$, $p < 0.001$; Fig. 9a) and 2 ($R^2 = 0.77$, RMSE = 3.95 $mW/m^2/nm/sr$, $p < 0.01$; Fig. 9b). The error between estimates was consistent across experiments, yielding RMSEs within 3.28–4.69 $mW/m^2/nm/sr$.

Low-resolution SCOPE-simulated $SIF_{760\text{-}3FLD}$ values (2- to 5.8-nm FWHM) were significantly correlated with $SIF_{760\text{-}3FLD}$ simulated at 1-nm FWHM ($p < 0.001$, R^2 0.70–0.99; Fig. 10). RMSE values tended to increase with decreasing SR (Fig. 10). The pattern of differing absolute $SIF_{760\text{-}3FLD}$ values but stable relative differences across SRs observed with the SCOPE-simulated data was consistent with the experimental results from the airborne hyperspectral imagers.

A comparison of airborne $SIF_{760\text{-}3FLD}$ retrievals to ground-based $SIF_{760\text{-}3FLD}$ retrievals in experiment 3 is shown in Fig. 11. Ground-based measures were significantly correlated with both the sub-nanometer ($R^2 = 0.90$, $p < 0.001$; Fig. 11a) and the narrow-band ($R^2 = 0.88$, $p < 0.001$) hyperspectral imagers (Fig. 11b). $SIF_{760\text{-}3FLD}$ from the sub-nanometer imager showed strong agreement with the ground-based $SIF_{760\text{-}3FLD}$ values (RMSE = 0.07 $mW/m^2/nm/sr$, rRMSE = 3.7%), whereas the narrow-band imager exhibited greater overall differences from ground-based measures (RMSE = 3.26 $mW/m^2/nm/sr$, rRMSE = 170.5%). SIF-yield, which was estimated by normalizing the corrected $SIF_{760\text{-}3FLD}$ by the average NIR radiance in the 776–780-nm spectral region, was also significantly correlated with the leaf-level steady-state chlorophyll fluorescence in experiment 1 ($R^2 = 0.53$, $p < 0.01$ for sub-nanometer imager; $R^2 = 0.34$, $p < 0.05$ for narrow-band imager).

Measures of O_2-A band depth and airborne $SIF_{760\text{-}3FLD}$ at different altitudes are presented in Fig. 12. $SIF_{760\text{-}3FLD}$ measures with the narrow-

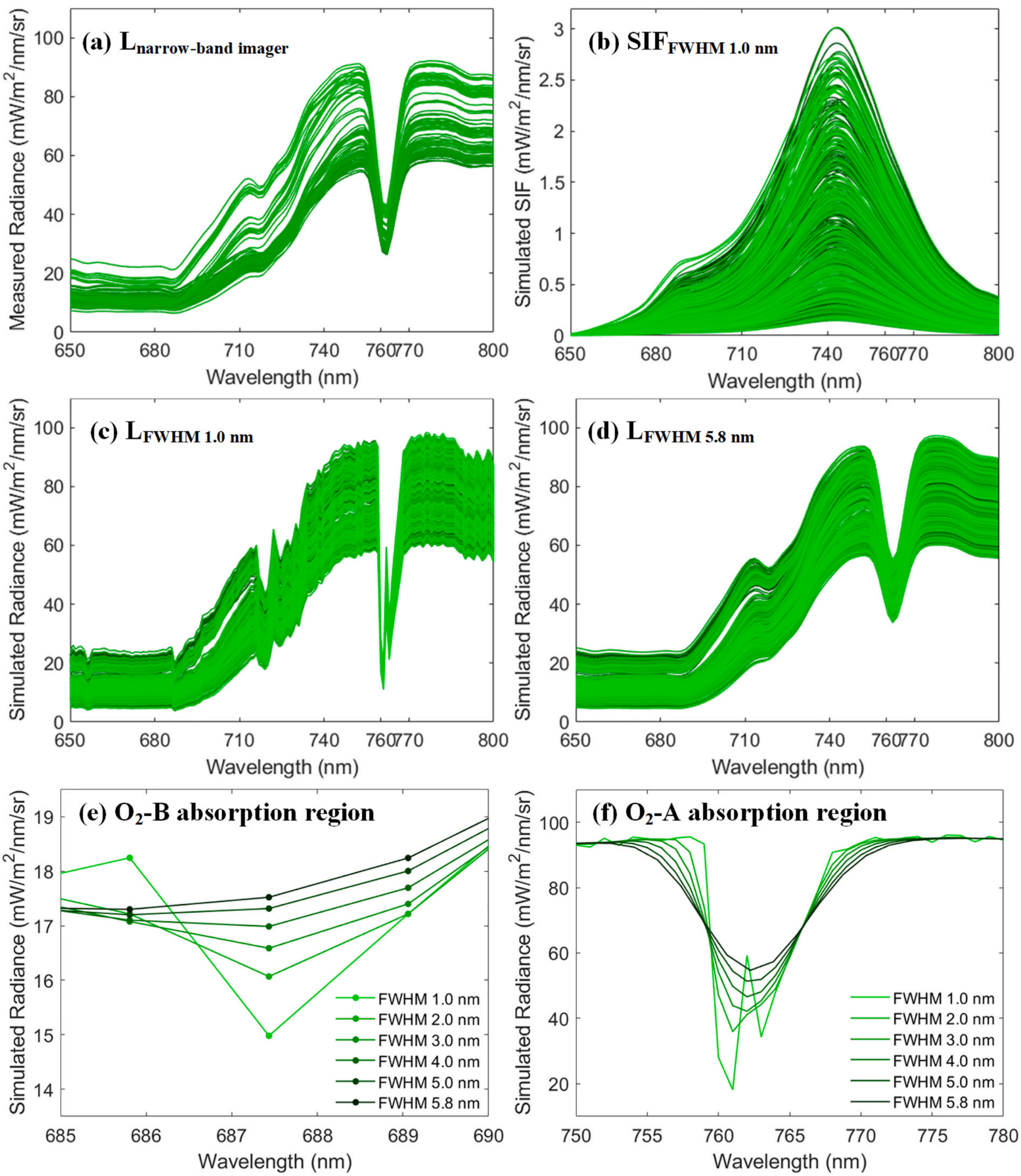

Fig. 5. (a) Measured radiance from the narrow-band imager. (b) SCOPE-simulated SIF at 1.0-nm FWHM. (c) SCOPE-simulated radiance at 1.0-nm FWHM. (d) SCOPE-simulated radiance corresponding to the narrow-band imager's spectral characteristics (FWHM = 5.8 nm, SSI = 1.626 nm). SCOPE-simulated radiance at different SRs in the O_2-B (e) and O_2-A absorption regions (f).

band imager at 2200 m AGL were excluded because pixels were too coarse (1.7 m) relative to plot size (3 m × 12 m). O_2-A absorption feature depth and $SIF_{760\text{-}3FLD}$ differed significantly with altitude (Fig. 12). The depth of the O_2-A absorption feature increased with sensor altitude, and $SIF_{760\text{-}3FLD}$ decreased with sensor altitude for both airborne imagers (Fig. 12).

Sub-nanometer $SIF_{760\text{-}3FLD}$ retrievals were significantly correlated with narrow-band imager retrievals in experiment 3 at both 900 m AGL ($R^2 = 0.85$, $p < 0.001$; Fig. 13a) and 1200 AGL ($R^2 = 0.9$, $p < 0.001$; Fig. 13a). The slope of the relationship between sub-nanometer and narrow-band retrievals was steeper for 900 m AGL than for 1200 m AGL. RMSE at 900 m AGL (4.29 mW/m^2/nm/sr) was higher than that of 1200 m AGL (3.28 mW/m^2/nm/sr), possibly explained by larger $SIF_{760\text{-}3FLD}$ values at lower altitudes. $SIF_{760\text{-}3FLD}$ at 900 m AGL was significantly correlated with $SIF_{760\text{-}3FLD}$ at 1200 m AGL ($R^2 = 0.92$, $p < 0.001$; Fig. 13b) and 2200 m AGL ($R^2 = 0.8$, $p < 0.001$; Fig. 13b) using the sub-nanometer imager. $SIF_{760\text{-}3FLD}$ values decreased with imager altitude, and the relationship between low-altitude and high-altitude measurements also changed, with shallower slopes at higher altitudes (Fig. 13b). RMSE was higher at 2200 m AGL than at 1200 m AGL altitude, when compared to 900 m AGL. A similar pattern was observed for narrow-band $SIF_{760\text{-}3FLD}$ retrievals, with an overall significant correlation (R^2

Table 5
Parameters and ranges used for the look-up table generation for the PRO4SAIL RTM.

Parameter	Abbreviation	Value/range
Chlorophyll $a + b$ content [μg/cm^2]	C_{ab}	4–70
Carotenoid content [μg/cm^2]	C_{x+c}	1–20
Anthocyanin content [μg/cm^2]	Anth	0–15
Dry matter content [g/cm^2]	C_m	0.007
Water content [g/cm^2]	C_w	0.001
Mesophyll structure Coeff.	N	0.5–3
Leaf area index [m^2/m^2]	LAI	0.3–5
Average leaf angle [deg.]	$LIDF_a$	0–90
Hot spot parameter	h	0.01
Soil reflectance	R_{soil}	PRO4SAIL dry soil spectra
Observer angle [deg.]	tt_o	0
Sun zenith angle [deg.]	tt_s	35.42
Relative azimuth angle [deg.]	Ψ	0

= 0.82, RMSE = 1.36 mW/m^2/nm/sr, $p < 0.001$; Fig. 13c) and lower $SIF_{760\text{-}3FLD}$ values at higher altitudes.

Sub-nanometer $SIF_{760\text{-}3FLD}$ was significantly correlated with ground-based $SIF_{760\text{-}3FLD}$ at all sensor altitudes ($p < 0.001$, all $R^2 > 0.9$; Fig. 14a). RMSEs between airborne and ground-based SIF retrievals at 900 and 1200 m AGL were lower than 0.1 mW/m^2/nm/sr and rRMSEs were lower than 4%. $SIF_{760\text{-}3FLD}$ at 2200 m AGL consistently underestimated ground-based SIF (RMSE = 0.5 mW/m^2/nm/sr and rRMSE = 28.2%; Fig. 14a). Ground-based $SIF_{760\text{-}3FLD}$ was also significantly correlated with airborne $SIF_{760\text{-}3FLD}$ from the narrow-band imager ($p < 0.001$, $R^2 > 0.85$) at both altitudes (Fig. 14b). Narrow-band imager $SIF_{760\text{-}3FLD}$ estimates at 1200 m AGL tended to be smaller than ground-based measures (Fig. 14b), and error was high for both 900 m AGL (RMSE = 3.77 mW/m^2/nm/sr, rRMSE = 200.8%) and 1200 m AGL (RMSE = 3.26 mW/m^2/nm/sr, rRMSE = 170.5%).

Nitrogen predictions from both RF models were significantly correlated ($p < 0.01$) with the field-level nitrogen content measurements obtained by destructive sampling (Fig. 15). $SIF_{760\text{-}FLD}$ from the sub-nanometer hyperspectral imager by itself was significantly correlated with field-level nitrogen content ($R^2 = 0.71$, $p < 0.001$; Fig. 15a), as was SIF_{760} quantified from the narrow-band imager ($R^2 = 0.67$, $p < 0.001$; Fig. 15b). The RF algorithm using $SIF_{760\text{-sub-nanometer}}$ performed slightly better ($R^2 = 0.93$, RMSE = 0.09%; Fig. 15c) than the RF using $SIF_{760\text{-narrow-band}}$ ($R^2 = 0.87$, RMSE = 0.12%; Fig. 15d).

4. Discussion

In this study we examined the relationship between airborne $SIF_{760\text{-}3FLD}$ quantified using sub-nanometer resolution (i.e., 0.1- to 0.2-nm FWHM) and narrow-band resolution (i.e., 5.8-nm FWHM) hyperspectral imagers in the context of plant phenotyping for homogenous crop canopies. Our results support the assertion that airborne SIF retrievals from narrow-band hyperspectral imagers can successfully track small physiological changes induced by plant pathogens and environmental stresses, as reported elsewhere (Calderón et al., 2015, 2013; Camino et al., 2021, 2018a; Hernández-Clemente et al., 2017; Panigada et al., 2014; Poblete et al., 2021, 2020; Zarco-Tejada et al., 2018, 2012). Precise SIF_{760} quantification at absolute scales was not essential for detecting plant stress in these studies. In our study, narrow-band airborne $SIF_{760\text{-}3FLD}$ was significantly associated with both sub-nanometer airborne and ground-based SIF observations. Our results particularly illustrate the capability of these narrow-band hyperspectral imagers for characterizing the intra-field SIF_{760} variability induced by different nitrogen fertilization rates.

Previous studies have highlighted the importance of sensor configuration for detecting spectral absorption features occurring over very narrow spectral ranges, particularly the need for high SR and SNR when quantifying SIF (Mohammed et al., 2019). The literature has emphasized the need for instruments with sub-nanometer resolutions to accurately characterize narrow absorption features for reliable SIF estimates in physical units (Cogliati et al., 2015; Julitta et al., 2016; Meroni and

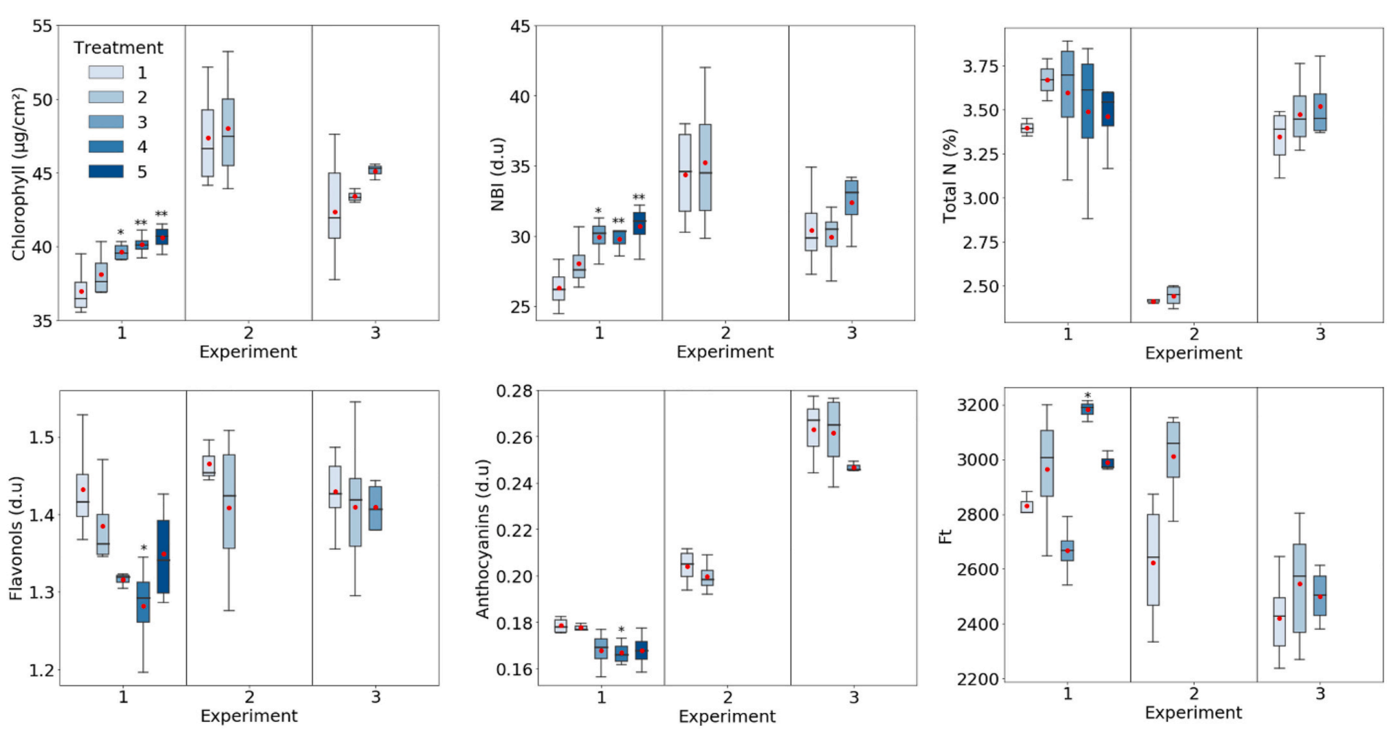

Fig. 6. Leaf physiological traits by fertilization rate across experiments. Average values indicated by red points. The black lines within boxes represent medians, and the top and bottom of each box represent the 75th and 25th quartile, respectively. Whiskers represent ±1.5 × Inter Quartile Range. Asterisks indicate significant differences from the treatment 1 plots according to Dunnett's test at $\alpha < 0.05$. *$p \leq 0.05$; **$p \leq 0.01$. (For interpretation of the references to colour in this figure legend, the reader is referred to the web version of this article.)

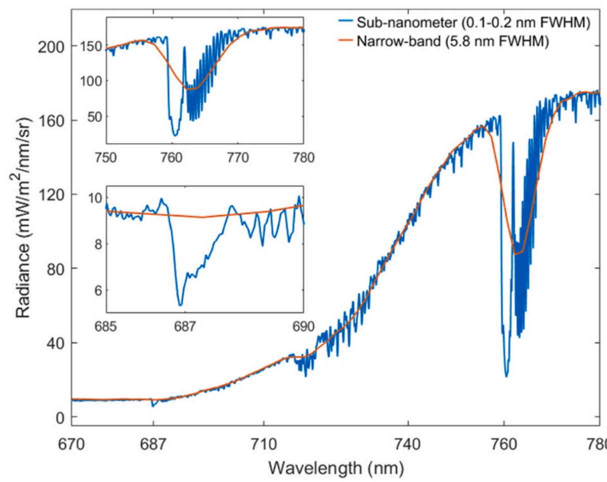

Fig. 7. Comparison of average radiance spectra from one of the plots within experiment-3 in the 670- to 780-nm region obtained from both hyperspectral imagers. The insets show the comparison within O_2-A and O_2-B absorption features in the 750- to 780-nm region and 685- to 690-nm region, respectively.

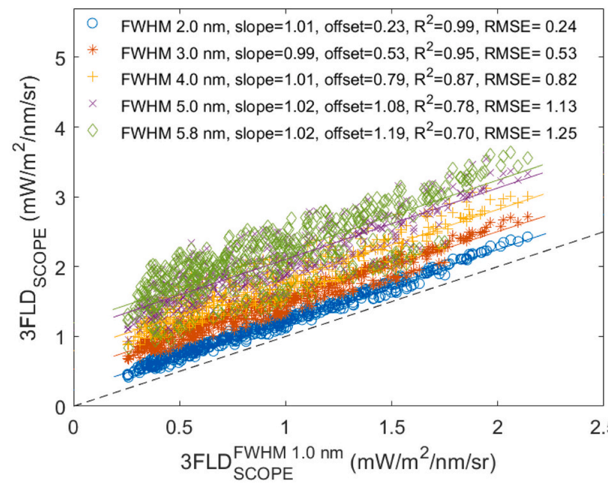

Fig. 10. Relationships between $SIF_{760\text{-}3FLD}$ for SCOPE simulations with different SRs against $SIF_{760\text{-}3FLD}$ quantified at 1.0-nm FWHM. The dotted line represents the 1:1 line.

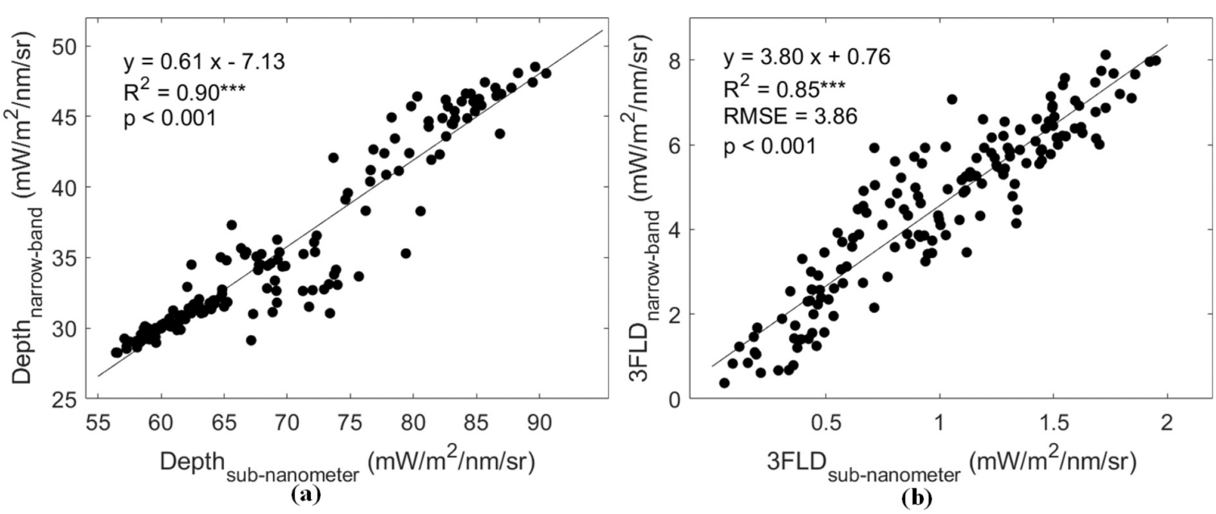

Fig. 8. Relationship between depth at the O_2-A absorption feature (a) and $SIF_{760\text{-}3FLD}$ (b) over the experimental field at site 1 from both hyperspectral imagers. The range of absolute $SIF_{760\text{-}3FLD}$ levels derived from the narrow-band imager was higher than the typical range of 0–3 $mW/m^2/nm/sr$ quantified from healthy vegetation due to the impact of the spectral resolution of the instrument.

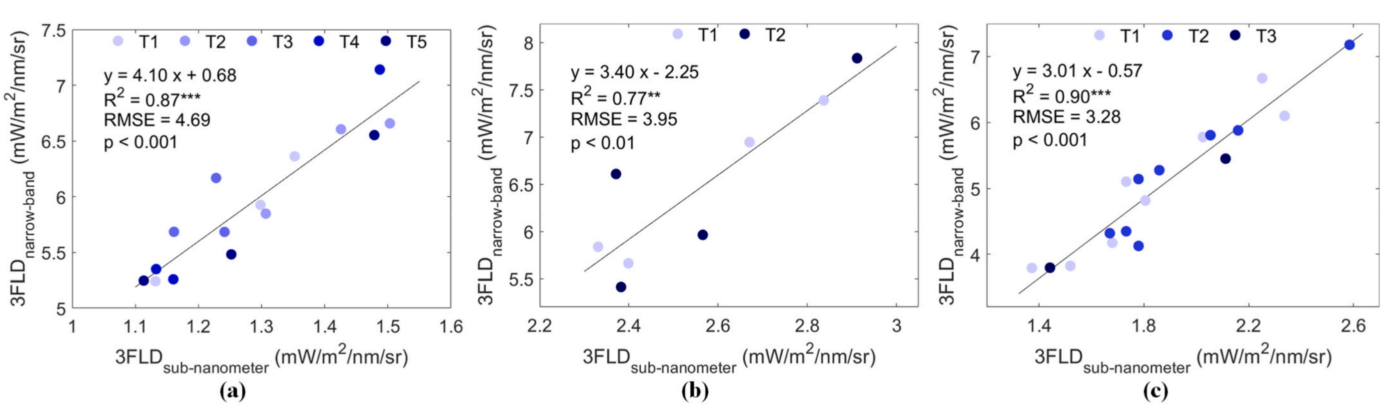

Fig. 9. Relationship between airborne $SIF_{760\text{-}3FLD}$ measures from different hyperspectral imagers across experiments 1 (a), 2 (b) and 3 (c). The range of absolute $SIF_{760\text{-}3FLD}$ levels derived from the narrow-band imager was higher than the typical range of 0–3 $mW/m^2/nm/sr$ quantified from healthy vegetation due to the impact of the spectral resolution of the instrument.

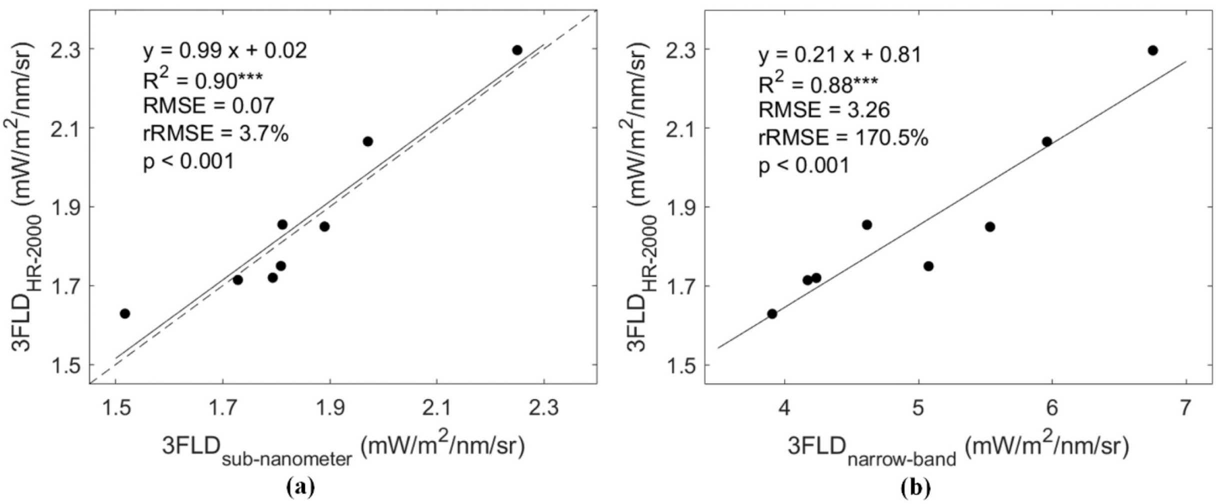

Fig. 11. Relationship between ground-based $SIF_{760\text{-}3FLD}$ quantified from the HR-2000 field spectrometer and airborne $SIF_{760\text{-}3FLD}$ quantified from the sub-nanometer (a) and the narrow-band (b) hyperspectral imagers for experiment 3. The dotted line represents the 1:1 line. The range of absolute $SIF_{760\text{-}3FLD}$ levels derived from the narrow-band imager was higher than the typical range of 0–3 mW/m^2/nm/sr quantified from healthy vegetation due to the impact of the spectral resolution of the instrument.

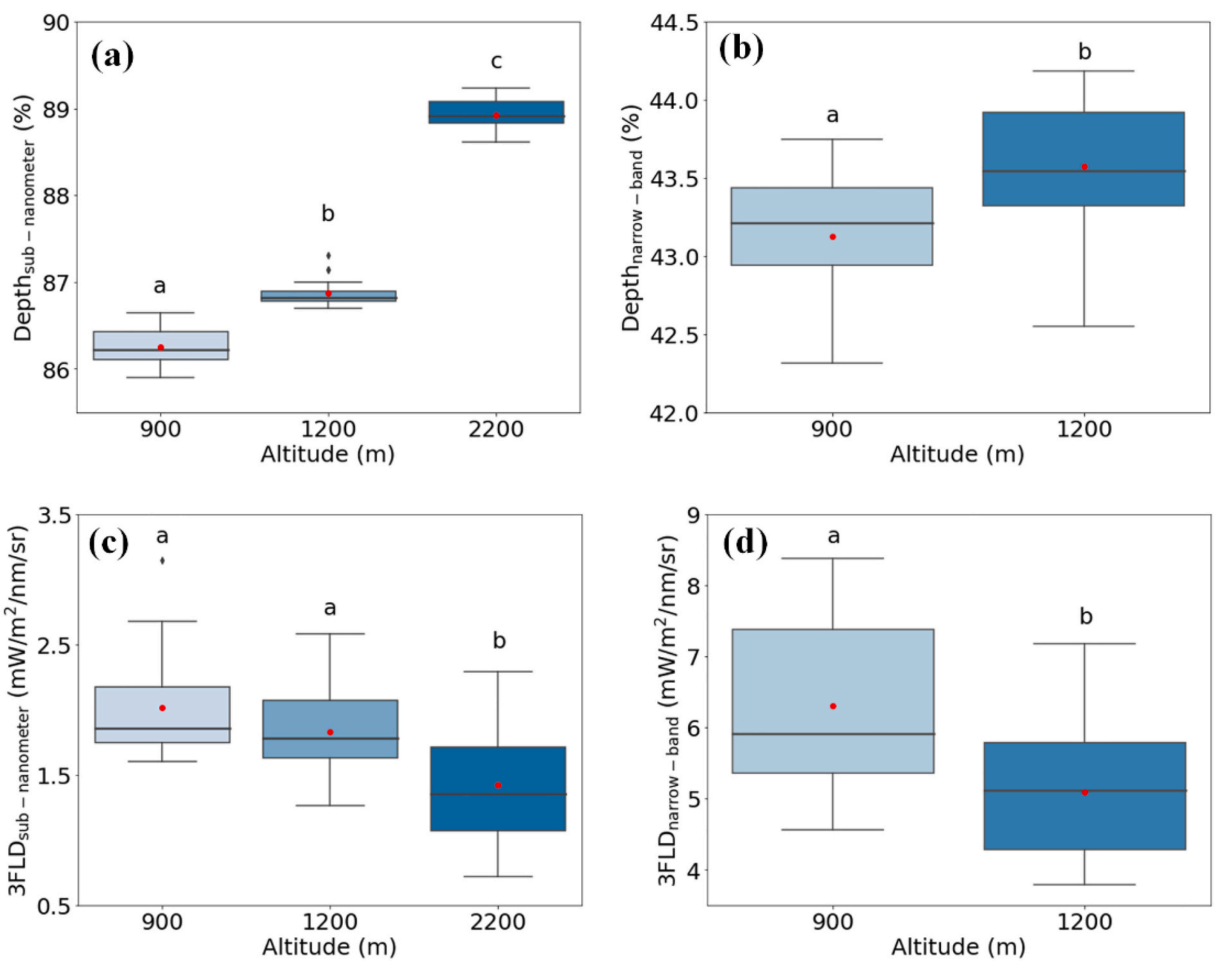

Fig. 12. Effect of sensor altitude on O_2-A band depth and $SIF_{760\text{-}3FLD}$ in experiment 3. Letters (a, b and c) within each plot represent the results of Tukey's honest significant difference (HSD) post-hoc comparisons of group means with $\alpha < 0.05$. Groups sharing the same letter are not significantly different. In the boxplots, the average values are shown with a red circle. The black line within the box is the median, and the top and bottom of the box is the 75th and 25th quartile, respectively. The whiskers represent $\pm 1.5 \times$ Interquartile range. The outliers are represented as diamonds. The range of absolute $SIF_{760\text{-}3FLD}$ levels derived from the narrow-band imager was higher than the typical range of 0–3 mW/m^2/nm/sr quantified from healthy vegetation due to the impact of the spectral resolution of the instrument. $SIF_{760\text{-}3FLD}$ measures with the narrow-band imager at 2200 m AGL were excluded because pixels were too coarse (1.7 m) relative to plot size (3 m × 12 m). (For interpretation of the references to colour in this figure legend, the reader is referred to the web version of this article.)

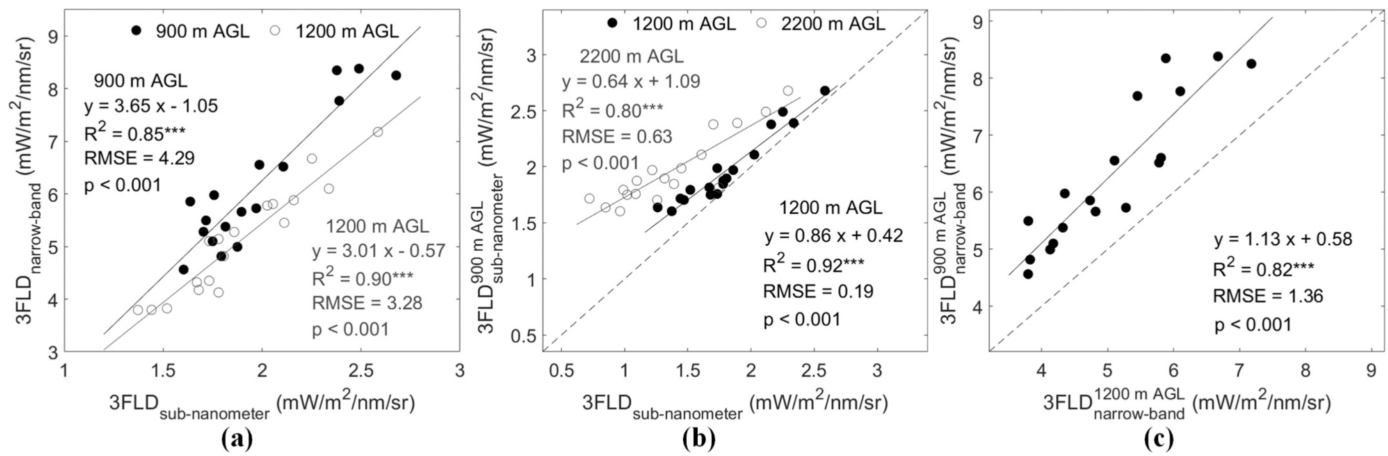

Fig. 13. (a) Relationships between $SIF_{760\text{-}3FLD}$ estimates from narrow-band and sub-nanometer hyperspectral imagers by sensor altitude. (b) Relationships between airborne $SIF_{760\text{-}3FLD}$ from sub-nanometer imager at 1200 and 2200 m AGL compared to the $SIF_{760\text{-}3FLD}$ quantified at 900 m AGL. (c) Relationship between airborne $SIF_{760\text{-}3FLD}$ from the narrow-band hyperspectral imager at 900 and 1200 m AGL. The range of absolute $SIF_{760\text{-}3FLD}$ levels derived from the narrow-band imager was higher than the typical range of 0–3 mW/m^2/nm/sr quantified from healthy vegetation due to the impact of the spectral resolution of the instrument. $SIF_{760\text{-}3FLD}$ measures with the narrow-band imager at 2200 m AGL were excluded because pixels were too coarse (1.7 m) relative to plot size (3 m × 12 m).

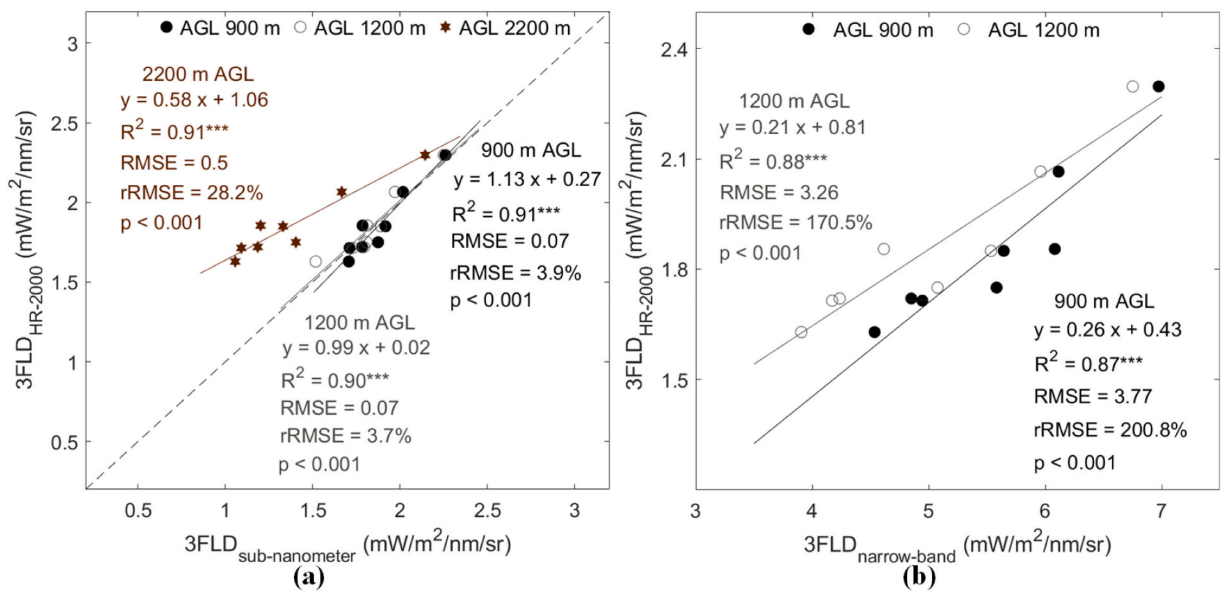

Fig. 14. Relationship between ground-based $SIF_{760\text{-}3FLD}$ quantified with a HR-2000 field spectrometer and airborne $SIF_{760\text{-}3FLD}$ at 900 m, 1200 m and 2200 m AGL retrieved from the sub-nanometer imager (a) and the narrow-band imager (b). The range of absolute $SIF_{760\text{-}3FLD}$ levels derived from the narrow-band imager was higher than the typical range of 0–3 mW/m^2/nm/sr quantified from healthy vegetation due to the impact of the spectral resolution of the instrument. $SIF_{760\text{-}3FLD}$ measures with the narrow-band imager at 2200 m AGL were excluded because pixels were too coarse (1.7 m) relative to plot size (3 m × 12 m).

Colombo, 2006; Meroni et al., 2011; Rossini et al., 2010). The experimental results from these studies are consistent with modelling studies based on FluorSAIL3 (Damm et al., 2011; Cendrero-Mateo et al., 2019) and SCOPE (Liu et al., 2015), which showed an increase in the SIF_{760} retrieval accuracy with increasing sensor SR. These modelling studies also found strong correlations between modelled and estimated SIF_{760} for low SR (5 nm) instruments using 3FLD ($r = 0.78$, RMSE $= 0.31$ mW/m^2/nm/sr) and iFLD ($r = 0.81$, RMSE $= 0.081$ mW/m^2/nm/sr) (Damm et al., 2011). The SCOPE modelling results presented in this study support the findings of previous modelling efforts, illustrating statistically significant relationships ($p < 0.001$, $R^2 = 0.70$–0.99, RMSE $= 0.24$–1.25 mW/m^2/nm/sr; Fig. 10) between $SIF_{760\text{-}3FLD}$ at 1 nm and $SIF_{760\text{-}3FLD}$ at coarser SRs ranging from 2-nm to 5.8-nm FWHM. The offset of the linear relationship with $SIF_{760\text{-}3FLD}$ at 1 nm increased steadily as the SR decreased from 2 to 5.8 nm, while the slope remained close to 1. This offset increase can be attributed to differences in radiance corresponding to the O_2-A band minima, which showed a 200% increase (Fig. 5f) when resampling radiance spectra from 1 to 5.8 nm SR. Our modelling results and those of previous studies suggest that narrow-band resolution sensors (4- to 6-nm FWHM) with sufficient SNR can sufficiently characterize relative SIF_{760} levels despite their inability to provide reliable absolute SIF_{760} estimates.

Differential nitrogen application rates in the three experiments were associated with variability of leaf physiological measurements (Fig. 6) and airborne $SIF_{760\text{-}3FLD}$. Narrow-band and sub-nanometer $SIF_{760\text{-}3FLD}$ estimates were strongly correlated across experiments, and both differed by nitrogen fertilization level. The best correlation, observed in experiment 3, may be attributed to the identical flight altitude at which the narrow-band and the sub-nanometer hyperspectral images were collected for this experiment (site 2; Table 2) in addition to the higher

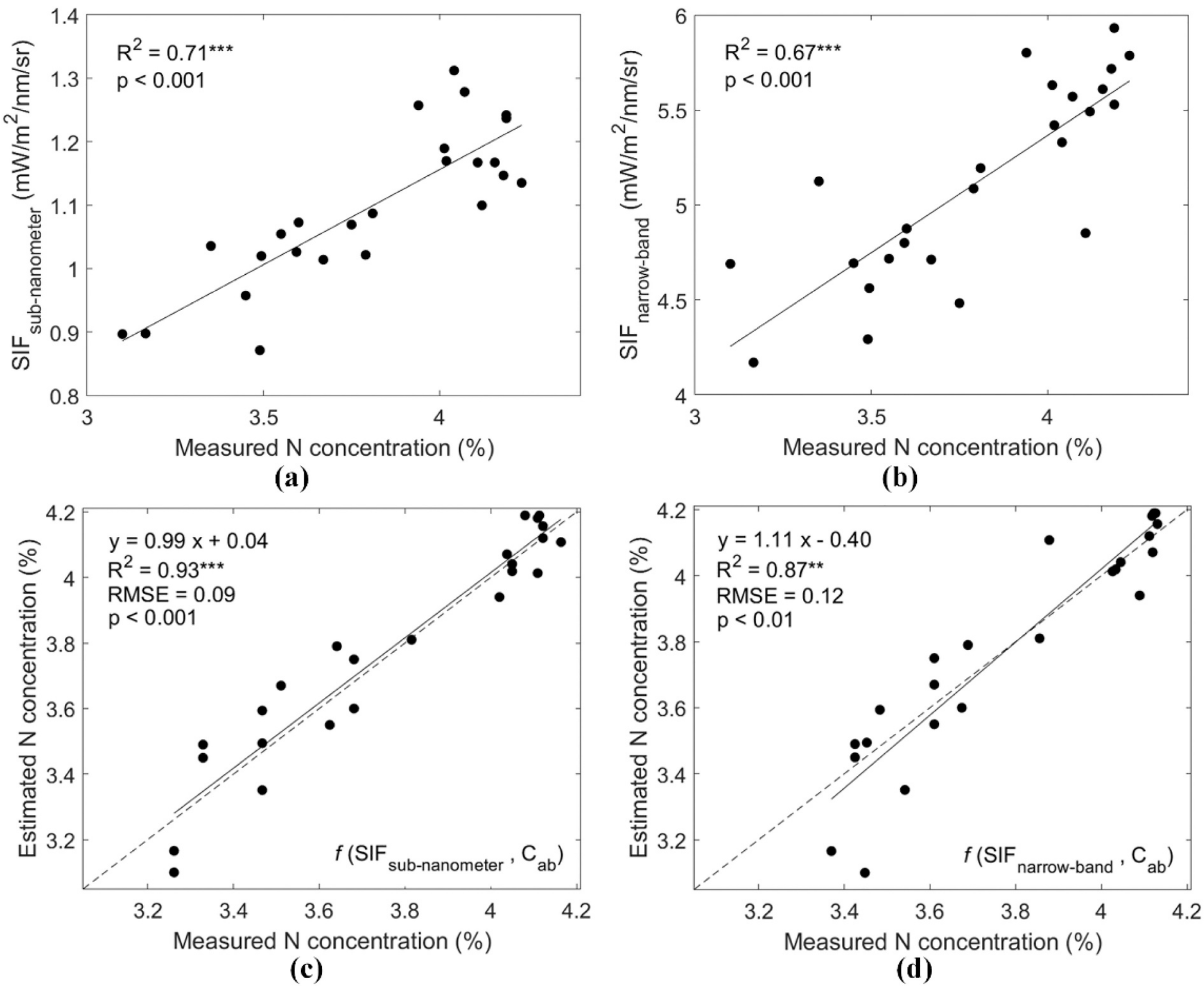

Fig. 15. Relationships between N concentration and airborne $SIF_{760\text{-}3FLD}$ quantified from a sub-nanometer (a) and narrow-band imager (b). Measured vs. estimated N concentration using Random Forest regression models, which included RTM-based C_{ab} and $SIF_{760\text{-}3FLD}$ generated from either a sub-nanometer (c) or narrow-band imager (d). The dotted line represents the 1:1 line. The range of absolute $SIF_{760\text{-}3FLD}$ levels derived from the narrow-band imager was higher than the typical range of 0–3 $mW/m^2/nm/sr$ quantified from healthy vegetation due to the impact of the spectral resolution of the instrument.

relative $SIF_{760\text{-}3FLD}$ variability observed within the experimental plots compared to experiments 1 and 2 (Fig. 9). The results demonstrated consistency across experimental sites and airborne campaigns carried out at different times, flight altitudes and years, showing robust relationships in terms of the relative $SIF_{760\text{-}3FLD}$ variability quantified by the two hyperspectral imagers. The differences obtained in absolute levels of $SIF_{760\text{-}3FLD}$ quantified in the three experiments can be associated with the differences in crop varieties, crop growth stages and the slightly different acquisition times of the airborne hyperspectral images. These results are consistent with previous studies showing differences in both ground-based and airborne SIF_{760} measurements according to nitrogen treatment (Cendrero-Mateo et al., 2016; Jia et al., 2018, 2021; Quemada et al., 2014; Watt et al., 2020a, 2020b).

Sensor altitude was identified as a critical factor in determining SIF accuracy (Daumard et al., 2015; Ni et al., 2016). MODTRAN (Berk et al., 2014) was used in these studies to show that the depth of the O_2-A absorption feature increases with sensor altitude. This is consistent with our findings, which show that the O_2-A band depth increased with altitude for both airborne hyperspectral imagers (Fig. 12) due to an increase in the radiance of the O_2-A band minima (Fig. 4h). Despite correcting for the atmospheric effects, $SIF_{760\text{-}3FLD}$ decreased with altitude for both airborne hyperspectral imagers. Such a decrease is linked to the correction method used, which relies on non-fluorescent targets. The relative increase in O_2-A band depth with increasing altitude is greater for vegetation targets than for bare soil targets (Daumard et al., 2015). This difference results in a bias in the corrected $SIF_{760\text{-}3FLD}$. Although $SIF_{760\text{-}3FLD}$ was overestimated at higher altitudes with both hyperspectral imagers, airborne estimates remained well correlated with ground-based measurements across altitudes (Figs. 12 and 14). This result has important implications for drone and airborne-based SIF quantifications in plant phenotyping studies and precision agriculture applications, in which sensor altitude is generally adapted depending on the flight efficiency and areal coverage. Although the relative variability needs to be assessed for detecting physiological changes induced by biotic or abiotic factors, understanding the effects of sensor altitude on SIF retrievals is critical for accurately interpreting SIF when used as input in stress-detection models.

Few studies have validated airborne-quantified SIF_{760} from narrow-band hyperspectral imagers against ground-based observations from high-resolution field spectrometers, due to the challenges associated with complex and heterogenous canopies including forest areas and cash crops such as vineyards and tree orchards. Damm et al. (2015) demonstrated the relationship between the medium-resolution Airborne Prism Experiment (APEX) sensor and a ground-based ASD (PANalytical, Boulder, US) field spectrometer for three different types of ecosystems. Measures were correlated ($R^2 = 0.71$), but airborne SIF_{760} systematically overestimated ground-based SIF_{760} by a proportionality factor (slope of airborne vs. ground SIF_{760} relationship) of 1.93 and an rRMSE of 28.9%. Guanter et al. (2007) found good agreement ($R^2 = 0.85$) between airborne SIF_{760} derived from the Compact Airborne Spectrographic Imager (CASI, Itres Research Ltd., Canada) and ground-based SIF_{760} derived from the ASD FieldSpec FR spectroradiometer. The airborne vs. ground-based relationship found in the current study ($R^2 = 0.88$, proportionality factor = 4.76) is consistent with the results from both studies above. Due to the impact of SR on the absolute $SIF_{760\text{-}3FLD}$ quantification, larger deviations in terms of rRMSE and proportionality factor were observed compared with the results from Damm et al. (2015), which can be attributed to the sub-nanometer resolution (0.065-nm FWHM) of the reference ground-based HR-2000 spectrometer used in our study as compared to the moderate spectral resolution of ASD spectrometers (>1.0-nm FWHM) used elsewhere.

The potential effects of the canopy structure are important to consider when comparing the narrow-band vs. sub-nanometer SIF retrievals. The TOC SIF observations from ground-based, airborne and spaceborne platforms are strongly affected by plant canopy structure due to the re-absorption and scattering of light within the canopy (Fournier et al., 2012; Porcar-Castell et al., 2014; Dechant et al., 2020; Yang and Van der Tol, 2018; Zeng et al., 2019). This structure is usually characterized by parameters such as leaf area index and the leaf inclination distribution function and may be approximated with vegetation indices such as Modified Triangular Vegetation Index (MTVI2) (Haboudane et al., 2004) and Enhanced Vegetation Index (EVI) (Huete et al., 2002) when assessing the effects of structure on SIF. In our study, the structural differences across experimental plots were generally small as structural changes were generally not associated with experimental treatments. Nevertheless, we tested whether treatment-associated variability in canopy structure could be related to $SIF_{760\text{-}3FLD}$ from the narrow-band hyperspectral imager. We found that the relationships of both MTVI2 and EVI with narrow-band airborne $SIF_{760\text{-}3FLD}$ were weak and non-significantly correlated at both field trial sites ($p > 0.1$, $R^2 = 0$–0.11; Fig. 16). These results suggest that the $SIF_{760\text{-}3FLD}$ variability captured by the narrow-band imager in the experiments was not driven by changes arising from structural effects. Moreover, it shows that the fluorescence *in-filling* at the O_2-A band was unaffected by structure, with the variability across experimental plots due to subtle physiological differences.

Predictive models of leaf N concentration improved only slightly when using SIF_{760} from the sub-nanometer imager compared to the narrow-band imager, with a marginal increase in the model performance ($R^2 = 0.87$ vs. 0.93) and a decrease in the error (RMSE = 0.12% vs. 0.09%). The direction of this improvement is consistent with the greater accuracy of the sub-nanometer SR imager. Nevertheless, these results suggest that data from the narrow-band hyperspectral imager may be sufficient for predicting N concentration in plant phenotyping and precision agriculture applications. Narrow-band imagery may be particularly suitable since relative changes in SIF linked to physiological conditions, nutritional deficiencies and stress levels are often the focus of such studies.

For assessing crop physiological status, standard commercially available hyperspectral imagers with 4- to 6-nm FWHM and SNRs greater than 300:1 can provide reliable relative SIF_{760} estimates (Zarco-Tejada et al., 2012, 2013a). These sensors are lightweight and can be carried on drone platforms that provide very high spatial resolution images due to low flying altitude. This capacity to generate very high spatial resolution imagery with narrow spectral bands is particularly important for plant phenotyping and precision agriculture applications for mapping physiological condition (Mohammed et al., 2019). Additional work using RTMs such as SCOPE and others is needed for improving the interpretation of SIF quantified using broader resolutions in precision agriculture.

5. Conclusions

We assessed the relationships between airborne $SIF_{760\text{-}3FLD}$ quantified from narrow-band (5.8-nm FWHM) and sub-nanometer (0.1- to 0.2-nm FWHM) hyperspectral imagers flown in tandem over three experimental fields with varying nitrogen application rates across 3 years. $SIF_{760\text{-}3FLD}$ estimates derived from each imager were significantly correlated with each other for all the three experiments ($p < 0.01$, $R^2 = 0.77$–0.90). Ground-level HR-2000 $SIF_{760\text{-}3FLD}$ was significantly correlated with that of the sub-nanometer ($p < 0.001$, $R^2 = 0.9$) and the narrow-band hyperspectral imager ($p < 0.001$, $R^2 = 0.88$). These strong correlations among the narrow-band, sub-nanometer and ground-based $SIF_{760\text{-}3FLD}$ retrievals support the use of narrow-band hyperspectral sensors for detecting relative SIF differences in the context of plant phenotyping, vegetation stress detection and plant physiological condition. Although sub-nanometer SR is required for the accurate retrieval of SIF in absolute units, broader-band hyperspectral imaging technology of 4- to 6-nm bandwidth used in this study provides reliable assessment of relative SIF_{760} variability. The broader-band hyperspectral technology is also cost-effective, compact and facilitates the collection of high-spatial resolution fluorescence data required in precision agriculture.

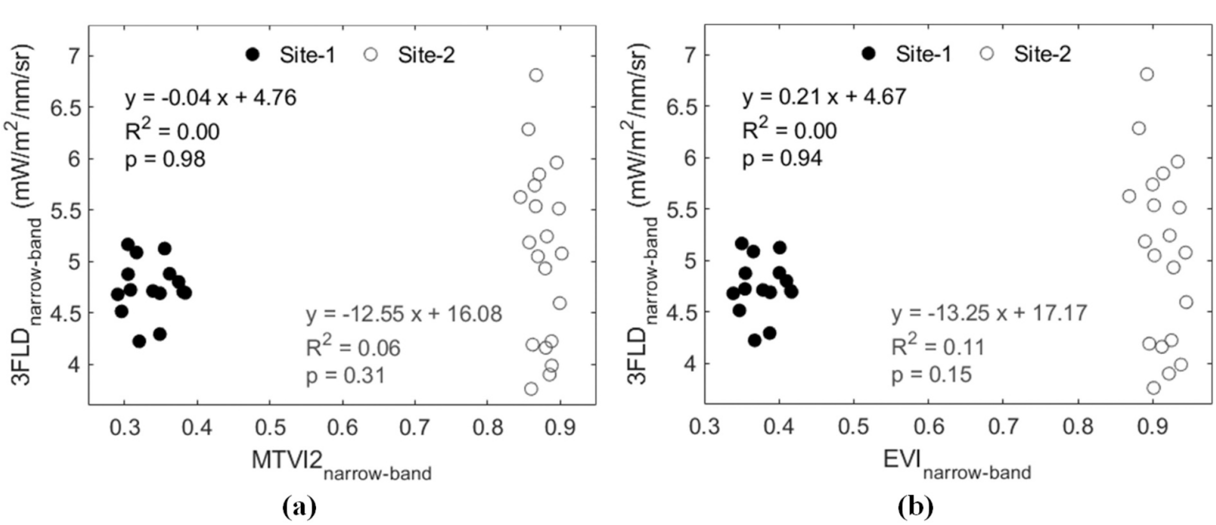

Fig. 16. Relationships between airborne $SIF_{760\text{-}3FLD}$ from the narrow-band hyperspectral imager and MTVI2 (a) and EVI (b). The range of absolute $SIF_{760\text{-}3FLD}$ levels derived from the narrow-band imager was higher than the typical range of 0–3 mW/m^2/nm/sr quantified from healthy vegetation due to the impact of the spectral resolution of the instrument.

Credit author statement

A.B., T.P. and P.J.Z.-T. designed the objectives of this study and designed research; A.B., T.P. and A.L. carried out field work and airborne data collections; A.B. analysed data and performed research; A. L. provided field support and access to experimental sites; A.B. wrote the paper, and T.P., A.H., R.H-C. and P.J.Z.-T. contributed and provided comments. All authors read and approved the final submission.

Declaration of Competing Interest

The authors declare that they have no known competing financial interests or personal relationships that could have appeared to influence the work reported in this paper.

Acknowledgements

The authors gratefully acknowledge the Foundation for Arable Research Australia, in particular Michael Straight and Ben Morris; the Grains Research and Development Corporation Australia; and Riverine Plains Incorporated for their provision and management of the field trials. A. Gracia-Romero and Y. Wang are acknowledged for their technical support during the field and airborne campaigns.

Appendix A. Supplementary data

Supplementary data to this article can be found online at https://doi.org/10.1016/j.rse.2022.112986.

References

Aasen, H., Honkavaara, E., Lucieer, A., Zarco-Tejada, P.J., 2018. Quantitative remote sensing at ultra-high resolution with UAV spectroscopy: a review of sensor technology, measurement procedures, and data correction workflows. Remote Sens. 10, 1091.
Badgley, G., Field, C.B., Berry, J.A., 2017. Canopy near-infrared reflectance and terrestrial photosynthesis. Sci. Adv. 3, e1602244.
Bandopadhyay, S., Rastogi, A., Rascher, U., Rademske, P., Schickling, A., Cogliati, S., Julitta, T., Arthur, A. Mac, Hueni, A., Tomelleri, E., Celesti, M., Burkart, A., Strózecki, M., Sakowska, K., Gabka, M., Rosadziński, S., Sojka, M., Iordache, M.D., Reusen, I., Van der Tol, C., Damm, A., Schuettemeyer, D., Juszczak, R., 2019. HyPlant-derived sun-induced fluorescence - a new opportunity to disentangle complex vegetation signals from diverse vegetation types. Remote Sens. 11, 1691.
Belwalkar, A., Poblete, T., Longmire, A., Hornero, A., Zarco-Tejada, P.J., 2021. Comparing the retrieval of chlorophyll fluorescence from two airborne hyperspectral imagers with different spectral resolutions for plant phenotyping studies. In: Proc. IEEE International Geoscience and Remote Sensing Symposium (IGARSS), 12–16 July 2021, Brussels, Belgium, pp. 5845–5848.
Berk, A., Conforti, P., Kennett, R., Perkins, T., Hawes, F., Van den Bosch, J., 2014. MODTRAN6: A major upgrade of the MODTRAN radiative transfer code. In: Proc. SPIE 9088, Algorithms and Technologies for Multispectral, Hyperspectral, and Ultraspectral Imagery XX, 90880H, 13 June 2014.
Breiman, L., 2001. Random Forests. Mach. Learn. 45, 5–32.
Calderón, R., Navas-Cortés, J.A., Lucena, C., Zarco-Tejada, P.J., 2013. High-resolution airborne hyperspectral and thermal imagery for early detection of Verticillium wilt of olive using fluorescence, temperature and narrow-band spectral indices. Remote Sens. Environ. 139, 231–245.
Calderón, R., Navas-Cortés, J.A., Zarco-Tejada, P.J., 2015. Early detection and quantification of Verticillium wilt in olive using hyperspectral and thermal imagery over large areas. Remote Sens. 7, 5584–5610.
Camino, C., Zarco-Tejada, P.J., Gonzalez-Dugo, V., 2018a. Effects of heterogeneity within tree crowns on airborne-quantified SIF and the CWSI as indicators of water stress in the context of precision agriculture. Remote Sens. 10, 604.
Camino, C., González-Dugo, V., Hernandez, P., Sillero, J.C., Zarco-Tejada, P.J., 2018b. Improved nitrogen retrievals with airborne-derived fluorescence and plant traits quantified from VNIR-SWIR hyperspectral imagery in the context of precision agriculture. Int. J. Appl. Earth Obs. Geoinf. 70, 105–117.
Camino, C., Gonzalez-Dugo, V., Hernandez, P., Zarco-Tejada, P.J., 2019. Radiative transfer Vcmax estimation from hyperspectral imagery and SIF retrievals to assess photosynthetic performance in rainfed and irrigated plant phenotyping trials. Remote Sens. Environ. 231, 111186.
Camino, C., Calderón, R., Parnell, S., Dierkes, H., Chemin, Y., Román-Écija, M., Montes-Borrego, M., Landa, B.B., Navas-Cortes, J.A., Zarco-Tejada, P.J., Beck, P.S.A., 2021. Detection of Xylella fastidiosa in almond orchards by synergic use of an epidemic spread model and remotely sensed plant traits. Remote Sens. Environ. 260, 112420.
Celesti, M., Van der Tol, C., Cogliati, S., Panigada, C., Yang, P., Pinto, F., Rascher, U., Miglietta, F., Colombo, R., Rossini, M., 2018. Exploring the physiological information of Sun-induced chlorophyll fluorescence through radiative transfer model inversion. Remote Sens. Environ. 215, 97–108.
Cendrero-Mateo, M.P., Moran, M.S., Papuga, S.A., Thorp, K.R., Alonso, L., Moreno, J., Ponce-Campos, G., Rascher, U., Wang, G., 2016. Plant chlorophyll fluorescence: active and passive measurements at canopy and leaf scales with different nitrogen treatments. J. Exp. Bot. 67, 275–286.
Cendrero-Mateo, M.P., Wieneke, S., Damm, A., Alonso, L., Pinto, F., Moreno, J., Guanter, L., Celesti, M., Rossini, M., Sabater, N., Cogliati, S., Julitta, T., Rascher, U., Goulas, Y., Aasen, H., Pacheco-Labrador, J., Mac Arthur, A., 2019. Sun-induced chlorophyll fluorescence III: benchmarking retrieval methods and sensor characteristics for proximal sensing. Remote Sens. 11, 962.
Cogliati, S., Rossini, M., Julitta, T., Meroni, M., Schickling, A., Burkart, A., Pinto, F., Rascher, U., Colombo, R., 2015. Continuous and long-term measurements of reflectance and sun-induced chlorophyll fluorescence by using novel automated field spectroscopy systems. Remote Sens. Environ. 164, 270–281.
Colombo, R., Celesti, M., Bianchi, R., Campbell, P.K.E., Cogliati, S., Cook, B.D., Corp, L. A., Damm, A., Domec, J.C., Guanter, L., Julitta, T., Middleton, E.M., Noormets, A., Panigada, C., Pinto, F., Rascher, U., Rossini, M., Schickling, A., 2018. Variability of sun-induced chlorophyll fluorescence according to stand age-related processes in a managed loblolly pine forest. Glob. Chang. Biol. 24, 2980–2996.
Damm, A., Erler, A., Hillen, W., Meroni, M., Schaepman, M.E., Verhoef, W., Rascher, U., 2011. Modeling the impact of spectral sensor configurations on the FLD retrieval accuracy of sun-induced chlorophyll fluorescence. Remote Sens. Environ. 115, 1882–1892.
Damm, A., Guanter, L., Laurent, V.C.E., Schaepman, M.E., Schickling, A., Rascher, U., 2014. FLD-based retrieval of sun-induced chlorophyll fluorescence from medium spectral resolution airborne spectroscopy data. Remote Sens. Environ. 147, 256–266.
Damm, A., Guanter, L., Paul-Limoges, E., Van der Tol, C., Hueni, A., Buchmann, N., Eugster, W., Ammann, C., Schaepman, M.E., 2015. Far-red sun-induced chlorophyll fluorescence shows ecosystem-specific relationships to gross primary production: an assessment based on observational and modeling approaches. Remote Sens. Environ. 166, 91–105.
Daumard, F., Goulas, Y., Champagne, S., Fournier, A., Ounis, A., Olioso, A., Moya, I., 2012. Continuous monitoring of canopy level sun-induced chlorophyll fluorescence during the growth of a sorghum field. IEEE Trans. Geosci. Remote Sens. 50, 4292–4300.
Daumard, F., Goulas, Y., Ounis, A., Pedrós, R., Moya, I., 2015. Measurement and correction of atmospheric effects at different altitudes for remote sensing of sun-induced fluorescence in oxygen absorption bands. IEEE Trans. Geosci. Remote Sens. 53, 5180–5196.
Dechant, B., Ryu, Y., Yang, K., Kim, J., 2017. A comprehensive analysis of spectral resolution effects on SIF retrieval and potential correction methods. In: Proc. American Geophysical Union, Fall Meeting, 11–15 December 2017, New Orleans, USA.
Dechant, B., Ryu, Y., Badgley, G., Zeng, Y., Berry, J.A., Zhang, Y., Goulas, Y., Li, Z., Zhang, Q., Kang, M., Li, J., Moya, I., 2020. Canopy structure explains the relationship between photosynthesis and sun-induced chlorophyll fluorescence in crops. Remote Sens. Environ. 241, 111733.
Drusch, M., Moreno, J., Del Bello, U., Franco, R., Goulas, Y., Huth, A., Kraft, S., Middleton, E.M., Miglietta, F., Mohammed, G., Nedbal, L., Rascher, U., Schüttemeyer, D., Verhoef, W., 2017. The FLuorescence EXplorer mission concept - ESA's Earth Explorer 8. IEEE Trans. Geosci. Remote Sens. 55, 1273–1284.
ESA (European Space Agency), 2015. Report for Mission Selection: FLEX. ESA SP-1330/2 (2 Volume Series). 197 pp., Noordwijk (The Netherlands). https://esamultimedia.esa.int/docs/EarthObservation/SP1330-2_FLEX.pdf.
Féret, J.B., Berger, K., de Boissieu, F., Malenovský, Z., 2021. PROSPECT-PRO for estimating content of nitrogen-containing leaf proteins and other carbon-based constituents. Remote Sens. Environ. 252, 112173.
Fournier, A., Daumard, F., Champagne, S., Ounis, A., Goulas, Y., Moya, I., 2012. Effect of canopy structure on sun-induced chlorophyll fluorescence. ISPRS J. Photogramm. Remote Sens. 68, 112–120.
Frankenberg, C., O'Dell, C., Berry, J., Guanter, L., Joiner, J., Köhler, P., Pollack, R., Taylor, T.E., 2014. Prospects for chlorophyll fluorescence remote sensing from the orbiting carbon observatory-2. Remote Sens. Environ. 147, 1–12.
Frankenberg, C., Köhler, P., Magney, T.S., Geier, S., Lawson, P., Schwochert, M., McDuffie, J., Drewry, D.T., Pavlick, R., Kuhnert, A., 2018. The chlorophyll fluorescence imaging spectrometer (CFIS), mapping far red fluorescence from aircraft. Remote Sens. Environ. 217, 523–536.
Gastellu-Etchegorry, J.-P., Lauret, N., Yin, T., Landier, L., Kallel, A., Malenovský, Z., Al Bitar, A., Aval, J., Benhmida, S., Qi, J., Medjdoub, G., Guilleux, J., Chavanon, E., Cook, B., Morton, D., Chrysoulakis, N., Mitraka, Z., 2017. DART: recent advances in remote sensing data modeling with atmosphere, polarization, and chlorophyll fluorescence. IEEE J. Sel. Top. Appl. Earth Obs. Remote Sens. 10, 2640–2649.
Genty, B., Briantais, J.M., Baker, N.R., 1989. The relationship between the quantum yield of photosynthetic electron transport and quenching of chlorophyll fluorescence. Biochim. Biophys. Acta 990, 87–92.
Gonzalez-Dugo, V., Hernandez, P., Solis, I., Zarco-Tejada, P.J., 2015. Using high-resolution hyperspectral and thermal airborne imagery to assess physiological condition in the context of wheat phenotyping. Remote Sens. 7, 13586–13605.
Grossmann, K., Frankenberg, C., Magney, T.S., Hurlock, S.C., Seibt, U., Stutz, J., 2018. PhotoSpec: a new instrument to measure spatially distributed red and far-red solar-induced chlorophyll fluorescence. Remote Sens. Environ. 216, 311–327.
Guanter, L., Alonso, L., Gómez-Chova, L., Amorós-López, J., Vila, J., Moreno, J., 2007. Estimation of solar-induced vegetation fluorescence from space measurements. Geophys. Res. Lett. 34, L08401.

Guanter, L., Alonso, L., Gómez-Chova, L., Meroni, M., Preusker, R., Fischer, J., Moreno, J., 2010. Developments for vegetation fluorescence retrieval from spaceborne high-resolution spectrometry in the O_2-A and O_2-B absorption bands. J. Geophys. Res. 115, 19303.

Guanter, L., Frankenberg, C., Dudhia, A., Lewis, P.E., Gómez-Dans, J., Kuze, A., Suto, H., Grainger, R.G., 2012. Retrieval and global assessment of terrestrial chlorophyll fluorescence from GOSAT space measurements. Remote Sens. Environ. 121, 236–251.

Guanter, L., Aben, I., Tol, P., Krijger, J.M., Hollstein, A., Köhler, P., Damm, A., Joiner, J., Frankenberg, C., Landgraf, J., 2015. Potential of the TROPOspheric Monitoring Instrument (TROPOMI) onboard the Sentinel-5 precursor for the monitoring of terrestrial chlorophyll fluorescence. Atmos. Meas. Tech. 8, 1337–1352.

Gueymard, C.A., 2001. Parameterized transmittance model for direct beam and circumsolar spectral irradiance. Sol. Energy 71, 325–346.

Haboudane, D., Miller, J.R., Pattey, E., Zarco-Tejada, P.J., Strachan, I.B., 2004. Hyperspectral vegetation indices and novel algorithms for predicting green LAI of crop canopies: modeling and validation in the context of precision agriculture. Remote Sens. Environ. 90, 337–352.

Hao, D., Zeng, Y., Qiu, H., Biriukova, K., Celesti, M., Migliavacca, M., Rossini, M., Asrar, G.R., Chen, M., 2021. Practical approaches for normalizing directional solar-induced fluorescence to a standard viewing geometry. Remote Sens. Environ. 255, 112171.

Hernández-Clemente, R., North, P.R.J., Hornero, A., Zarco-Tejada, P.J., 2017. Assessing the effects of forest health on sun-induced chlorophyll fluorescence using the FluorFLIGHT 3-D radiative transfer model to account for forest structure. Remote Sens. Environ. 193, 165–179.

Hornero, A., North, P.R.J., Zarco-Tejada, P.J., Rascher, U., Martín, M.P., Migliavacca, M., Hernández-Clemente, R., 2021a. Assessing the contribution of understory sun-induced chlorophyll fluorescence through 3-D radiative transfer modelling and field data. Remote Sens. Environ. 253, 112195.

Hornero, A., Zarco-Tejada, P.J., Quero, J.L., North, P.R.J., Ruiz-Gómez, F.J., Sánchez-Cuesta, R., Hernández-Clemente, R., 2021b. Modelling hyperspectral- and thermal-based plant traits for the early detection of Phytophthora-induced symptoms in oak decline. Remote Sens. Environ. 263, 112570.

Huete, A., Didan, K., Miura, T., Rodriguez, E.P., Gao, X., Ferreira, L.G., 2002. Overview of the radiometric and biophysical performance of the MODIS vegetation indices. Remote Sens. Environ 83, 195–213.

Jacquemoud, S., Baret, F., 1990. PROSPECT: a model of leaf optical properties spectra. Remote Sens. Environ. 34, 75–91.

Jia, M., Zhu, J., Ma, C., Alonso, L., Li, D., Cheng, T., Tian, Y., Zhu, Y., Yao, X., Cao, W., 2018. Difference and potential of the upward and downward sun-induced chlorophyll fluorescence on detecting leaf nitrogen concentration in wheat. Remote Sens. 10, 1315.

Jia, M., Colombo, R., Rossini, M., Celesti, M., Zhu, J., Cogliati, S., Cheng, T., Tian, Y., Zhu, Y., Cao, W., Yao, X., 2021. Estimation of leaf nitrogen content and photosynthetic nitrogen use efficiency in wheat using sun-induced chlorophyll fluorescence at the leaf and canopy scales. Eur. J. Agron. 122, 126192.

Julitta, T., Corp, L.A., Rossini, M., Burkart, A., Cogliati, S., Davies, N., Hom, M., Arthur, A. Mac, Middleton, E.M., Rascher, U., Schickling, A., Colombo, R., 2016. Comparison of sun-induced chlorophyll fluorescence estimates obtained from four portable field spectroradiometers. Remote Sens. 8, 122.

Julitta, T., Wutzler, T., Rossini, M., Colombo, R., Cogliati, S., Meroni, M., Burkart, A., Migliavacca, M., 2017. An R package for field spectroscopy: From system characterization to sun-induced chlorophyll fluorescence retrieval. In: Proc. 6th International Workshop on Remote Sensing of Vegetation Fluorescence, 17–19 January 2017, Frascatti, Italy.

Kim, J., Ryu, Y., Dechant, B., Lee, H., Kim, H.S., Kornfeld, A., Berry, J.A., 2021. Solar-induced chlorophyll fluorescence is non-linearly related to canopy photosynthesis in a temperate evergreen needleleaf forest during the fall transition. Remote Sens. Environ. 258, 112362.

Kjeldahl, J., 1883. Neue Methode zur Bestimmung des Stickstoffs in organischen. J. Anal. Chem. 22, 366–382.

Krause, G.H., Weis, E., 1984. Chlorophyll fluorescence as a tool in plant physiology. II. Interpretation of fluorescence signals. Photosynth. Res. 5, 139–157.

Li, Z., Zhang, Q., Li, J., Yang, X., Wu, Y., Zhang, Z., Wang, S., Wang, H., Zhang, Y., 2020. Solar-induced chlorophyll fluorescence and its link to canopy photosynthesis in maize from continuous ground measurements. Remote Sens. Environ. 236, 111420.

Lichtenthaler, H.K., Rinderle, U., 1988. The role of chlorophyll fluorescence in the detection of stress conditions in plants. Crit. Rev. Anal. Chem. 19 (Suppl. 1), S29–S85.

Liu, L., Liu, X., Hu, J., 2015. Effects of spectral resolution and SNR on the vegetation solar-induced fluorescence retrieval using FLD-based methods at canopy level. Eur. J. Remote Sens. 48, 743–762.

Maier, S.W., Günther, K.P., Stellmes, M., 2003. Sun-induced fluorescence: a new tool for precision farming. In: Schepers, J., VanToai, T. (Eds.), Digital Imaging and Spectral Techniques: Applications to Precision Agriculture and Crop Physiology. ASA Spec. Publ. 66. ASA, CSSA, and SSSA, Madison (Wisconsin), USA, pp. 209–222.

Marrs, J.K., Jones, T.S., Allen, D.W., Hutyra, L.R., 2021. Instrumentation sensitivities for tower-based solar-induced fluorescence measurements. Remote Sens. Environ. 259, 112413.

Meroni, M., Colombo, R., 2006. Leaf level detection of solar induced chlorophyll fluorescence by means of a subnanometer resolution spectroradiometer. Remote Sens. Environ. 103, 438–448.

Meroni, M., Rossini, M., Guanter, L., Alonso, L., Rascher, U., Colombo, R., Moreno, J., 2009. Remote sensing of solar-induced chlorophyll fluorescence: review of methods and applications. Remote Sens. Environ. 113, 2037–2051.

Meroni, M., Busetto, L., Colombo, R., Guanter, L., Moreno, J., Verhoef, W., 2010. Performance of spectral fitting methods for vegetation fluorescence quantification. Remote Sens. Environ. 114, 363–374.

Meroni, M., Barducci, A., Cogliati, S., Castagnoli, F., Rossini, M., Busetto, L., Di Cella, U. M., 2011. The hyperspectral irradiometer, a new instrument for long-term and unattended field spectroscopy measurements. Rev. Sci. Instrum. 82, 043106.

Mohammed, G.H., Colombo, R., Middleton, E.M., Rascher, U., Van der Tol, C., Nedbal, L., Goulas, Y., Pérez-Priego, O., Damm, A., Meroni, M., Joiner, J., Cogliati, S., Verhoef, W., Malenovský, Z., Gastellu-Etchegorry, J.P., Miller, J.R., Guanter, L., Moreno, J., Moya, I., Berry, J.A., Frankenberg, C., Zarco-Tejada, P.J., 2019. Remote sensing of solar-induced chlorophyll fluorescence (SIF) in vegetation: 50 years of progress. Remote Sens. Environ. 231, 111177.

Nakashima, N., Kato, T., Morozumi, T., Tsujimoto, K., Akitsu, T.K., Nasahara, K.N., Murayama, S., Muraoka, H., Noda, H.M., 2021. Area-ratio Fraunhofer line depth (aFLD) method approach to estimate solar-induced chlorophyll fluorescence in low spectral resolution spectra in a cool-temperate deciduous broadleaf forest. J. Plant Res. 134, 713–728.

Ni, Z., Liu, Z., Li, Z.L., Nerry, F., Huo, H., Sun, R., Yang, P., Zhang, W., 2016. Investigation of atmospheric effects on retrieval of sun-induced fluorescence using hyperspectral imagery. Sensors 16, 480.

Nichol, C.J., Drolet, G., Porcar-Castell, A., Wade, T., Sabater, N., Middleton, E.M., Maclellan, C., Levula, J., Mammarella, I., Vesala, T., Atherton, J., 2019. Diurnal and seasonal solar induced chlorophyll fluorescence and photosynthesis in a boreal scots pine canopy. Remote Sens. 11, 273.

Panigada, C., Rossini, M., Meroni, M., Cilia, C., Busetto, L., Amaducci, S., Boschetti, M., Cogliati, S., Picchi, V., Pinto, F., Marchesi, A., Colombo, R., 2014. Fluorescence, PRI and canopy temperature for water stress detection in cereal crops. Int. J. Appl. Earth Obs. Geoinf. 30, 167–178.

Pedrós, R., Moya, I., Goulas, Y., Jacquemoud, S., 2008. Chlorophyll fluorescence emission spectrum inside a leaf. Photochem. Photobiol. Sci. 7, 498–502.

Pérez-Priego, O., Zarco-Tejada, P.J., Miller, J.R., Sepulcre-Cantó, G., Fereres, E., 2005. Detection of water stress in orchard trees with a high-resolution spectrometer through chlorophyll fluorescence *in-filling* of the O_2-A band. IEEE Trans. Geosci. Remote Sens. 43, 2860–2869.

Plascyk, J.A., 1975. The MK II Fraunhofer line discriminator (FLD-II) for airborne and orbital remote sensing of solar-stimulated luminescence. Opt. Eng. 14, 144339.

Poblete, T., Camino, C., Beck, P.S.A., Hornero, A., Kattenborn, T., Saponari, M., Boscia, D., Navas-Cortes, J.A., Zarco-Tejada, P.J., 2020. Detection of Xylella fastidiosa infection symptoms with airborne multispectral and thermal imagery: assessing bandset reduction performance from hyperspectral analysis. ISPRS J. Photogramm. Remote Sens. 162, 27–40.

Poblete, T., Navas-Cortes, J.A., Camino, C., Calderon, R., Hornero, A., Gonzalez-Dugo, V., Landa, B.B., Zarco-Tejada, P.J., 2021. Discriminating *Xylella fastidiosa* from *Verticillium dahliae* infections in olive trees using thermal- and hyperspectral-based plant traits. ISPRS J. Photogramm. Remote Sens. 179, 133–144.

Porcar-Castell, A., Tyystjärvi, E., Atherton, J., Van der Tol, C., Flexas, J., Pfündel, E.E., Moreno, J., Frankenberg, C., Berry, J.A., 2014. Linking chlorophyll a fluorescence to photosynthesis for remote sensing applications: mechanisms and challenges. J. Exp. Bot 65, 4065–4095.

Quemada, M., Gabriel, J.L., Zarco-Tejada, P., 2014. Airborne hyperspectral images and ground-level optical sensors as assessment tools for maize nitrogen fertilization. Remote Sens. 6, 2940–2962.

Rascher, U., Alonso, L., Burkart, A., Cilia, C., Cogliati, S., Colombo, R., Damm, A., Drusch, M., Guanter, L., Hanus, J., Hyvärinen, T., Julitta, T., Jussila, J., Kataja, K., Kokkalis, P., Kraft, S., Kraska, T., Matveeva, M., Moreno, J., Muller, O., Panigada, C., Pikl, M., Pinto, F., Prey, L., Pude, R., Rossini, M., Schickling, A., Schurr, U., Schüttemeyer, D., Verrelst, J., Zemek, F., 2015. Sun-induced fluorescence - a new probe of photosynthesis: first maps from the imaging spectrometer HyPlant. Glob. Chang. Biol. 21, 4673–4684.

Rossini, M., Meroni, M., Migliavacca, M., Manca, G., Cogliati, S., Busetto, L., Picchi, V., Cescatti, A., Seufert, G., Colombo, R., 2010. High resolution field spectroscopy measurements for estimating gross ecosystem production in a rice field. Agric. For. Meteorol. 150, 1283–1296.

Rossini, M., Meroni, M., Celesti, M., Cogliati, S., Julitta, T., Panigada, C., Rascher, U., Van der Tol, C., Colombo, R., 2016. Analysis of red and far-red sun-induced chlorophyll fluorescence and their ratio in different canopies based on observed and modeled data. Remote Sens. 8, 412.

Siegmann, B., Alonso, L., Celesti, M., Cogliati, S., Colombo, R., Damm, A., Douglas, S., Guanter, L., Hanuš, J., Kataja, K., Kraska, T., Matveeva, M., Moreno, J., Muller, O., Pikl, M., Pinto, F., Vargas, J.Q., Rademske, P., Rodriguez-Morene, F., Sabater, N., Schickling, A., Schüttemeyer, D., Zemek, F., Rascher, U., 2019. The high-performance airborne imaging spectrometer HyPlant-from raw images to top-of-canopy reflectance and fluorescence products: introduction of an automatized processing chain. Remote Sens. 11, 2760.

Suarez, L., Gonzalez-Dugo, V., Camino, C., Hornero, A., Zarco-Tejada, P.J., 2021. Physical model inversion of the green spectral region to track assimilation rate in almond trees with an airborne nano-hyperspectral imager. Remote Sens. Environ. 252, 112147.

Sun, Y., Frankenberg, C., Wood, J.D., Schimel, D.S., Jung, M., Guanter, L., Drewry, D.T., Verma, M., Porcar-Castell, A., Griffis, T.J., Gu, L., Magney, T.S., Köhler, P., Evans, B., Yuen, K., 2017. OCO-2 advances photosynthesis observation from space via solar induced chlorophyll fluorescence. Science 358 eaam5747.

Süß, A., Hank, T., Mauser, W., 2016. Deriving diurnal variations in sun-induced chlorophyll-a fluorescence in winter wheat canopies and maize leaves from ground-based hyperspectral measurements. Int. J. Remote Sens. 37, 60–77.

Tagliabue, G., Panigada, C., Celesti, M., Cogliati, S., Colombo, R., Migliavacca, M., Rascher, U., Rocchini, D., Schüttemeyer, D., Rossini, M., 2020. Sun–induced fluorescence heterogeneity as a measure of functional diversity. Remote Sens. Environ. 247, 111934.

Van der Tol, C., Verhoef, W., Timmermans, J., Verhoef, A., Su, Z., 2009. An integrated model of soil-canopy spectral radiances, photosynthesis, fluorescence, temperature and energy balance. Biogeosci 6, 3109–3129.

Verhoef, W., 1984. Light scattering by leaf layers with application to canopy reflectance modeling: the SAIL model. Remote Sens. Environ. 16, 125–141.

Verhoef, W., 2004. Extension of SAIL to model solar - induced canopy fluorescence spectra. In: Proc. 2nd International Workshop on Remote Sensing of Vegetation Fluorescence, 17–19 November 2004, Montreal, Canada.

Verhoef, W., Jia, L., Xiao, Q., Su, Z., 2007. Unified optical-thermal four-stream radiative transfer theory for homogeneous vegetation canopies. IEEE Trans. Geosci. Remote Sens. 45, 1808–1822.

Verhoef, W., Van der Tol, C., Middleton, E.M., 2018. Hyperspectral radiative transfer modeling to explore the combined retrieval of biophysical parameters and canopy fluorescence from FLEX – Sentinel-3 tandem mission multi-sensor data. Remote Sens. Environ. 204, 942–963.

Vilfan, N., Van der Tol, C., Muller, O., Rascher, U., Verhoef, W., 2016. Fluspect-B: a model for leaf fluorescence, reflectance and transmittance spectra. Remote Sens. Environ. 186, 596–615.

Wang, Y., Suarez, L., Qian, X., Poblete, T., Gonzalez-Dugo, V., Ryu, D., Zarco-Tejada, P. J., 2021. Assessing the contribution of airborne-retrieved chlorophyll fluorescence for nitrogen assessment in almond orchards. In: Proc. IEEE International Geoscience and Remote Sensing Symposium (IGARSS), 12–16 July 2021, Brussels, Belgium, pp. 5853–5856.

Watt, M.S., Buddenbaum, H., Leonardo, E.M.C., Estarija, H.J., Bown, H.E., Gomez-Gallego, M., Hartley, R.J.L., Pearse, G.D., Massam, P., Wright, L., Zarco-Tejada, P.J., 2020a. Monitoring biochemical limitations to photosynthesis in N and P-limited radiata pine using plant functional traits quantified from hyperspectral imagery. Remote Sens. Environ. 248, 112003.

Watt, M.S., Buddenbaum, H., Leonardo, E.M.C., Estarija, H.J.C., Bown, H.E., Gomez-Gallego, M., Hartley, R., Massam, P., Wright, L., Zarco-Tejada, P.J., 2020b. Using hyperspectral plant traits linked to photosynthetic efficiency to assess N and P partition. ISPRS J. Photogramm. Remote Sens. 169, 406–420.

Weis, E., Berry, J.A., 1987. Quantum efficiency of photosystem II in relation to 'energy'-dependent quenching of chlorophyll fluorescence. Biochim. Biophys. Acta 894, 198–208.

Wieneke, S., Ahrends, H., Damm, A., Pinto, F., Stadler, A., Rossini, M., Rascher, U., 2016. Airborne based spectroscopy of red and far-red sun-induced chlorophyll fluorescence: implications for improved estimates of gross primary productivity. Remote Sens. Environ. 184, 654–667.

Yang, P., Van der Tol, C., 2018. Linking canopy scattering of far-red sun-induced chlorophyll fluorescence with reflectance. Remote Sens. Environ. 209, 456–467.

Yang, R., Juhasz, A., Zhang, Yujuan, Chen, X., Zhang, Yinjun, She, M., Zhang, J., Maddern, R., Edwards, I., Diepeveen, D., Islam, S., Ma, W., 2018. Molecular characterisation of the NAM-1 genes in bread wheat in Australia. Crop Pastur. Sci. 69, 1173–1181.

Zarco-Tejada, P.J., Miller, J.R., Mohammed, G.H., Noland, T.L., 2000a. Chlorophyll fluorescence effects on vegetation apparent reflectance: I. Leaf-level measurements and model simulation. Remote Sens. Environ. 74, 582–595.

Zarco-Tejada, P.J., Miller, J.R., Mohammed, G.H., Noland, T.L., Sampson, P.H., 2000b. Chlorophyll fluorescence effects on vegetation apparent reflectance: II. Laboratory and airborne canopy-level measurements with hyperspectral data. Remote Sens. Environ. 74, 596–608.

Zarco-Tejada, P.J., González-Dugo, V., Berni, J.A.J., 2012. Fluorescence, temperature and narrow-band indices acquired from a UAV platform for water stress detection using a micro-hyperspectral imager and a thermal camera. Remote Sens. Environ. 117, 322–337.

Zarco-Tejada, P.J., Catalina, A., González, M.R., Martín, P., 2013a. Relationships between net photosynthesis and steady-state chlorophyll fluorescence retrieved from airborne hyperspectral imagery. Remote Sens. Environ. 136, 247–258.

Zarco-Tejada, P.J., Suarez, L., Gonzalez-Dugo, V., 2013b. Spatial resolution effects on chlorophyll fluorescence retrieval in a heterogeneous canopy using hyperspectral imagery and radiative transfer simulation. IEEE Geosci. Remote Sens. Lett. 10, 937–941.

Zarco-Tejada, P.J., González-Dugo, M.V., Fereres, E., 2016. Seasonal stability of chlorophyll fluorescence quantified from airborne hyperspectral imagery as an indicator of net photosynthesis in the context of precision agriculture. Remote Sens. Environ. 179, 89–103.

Zarco-Tejada, P.J., Camino, C., Beck, P.S.A., Calderon, R., Hornero, A., Hernández-Clemente, R., Kattenborn, T., Montes-Borrego, M., Susca, L., Morelli, M., Gonzalez-Dugo, V., North, P.R.J., Landa, B.B., Boscia, D., Saponari, M., Navas-Cortes, J.A., 2018. Previsual symptoms of Xylella fastidiosa infection revealed in spectral plant-trait alterations. Nat. Plant 4, 432–439.

Zeng, Y., Badgley, G., Dechant, B., Ryu, Y., Chen, M., Berry, J.A., 2019. A practical approach for estimating the escape ratio of solar-induced chlorophyll fluorescence. Remote Sens. Environ. 232, 111209.

Zhao, F., Dai, X., Verhoef, W., Guo, Y., Van der Tol, C., Li, Y., Huang, Y., 2016. FluorWPS: a Monte Carlo ray-tracing model to compute sun-induced chlorophyll fluorescence of three-dimensional canopy. Remote Sens. Environ. 187, 385–399.